






3D bioprinted dynamic bioactive living construct enhances mechanotransduction-assisted rapid neural network self-organization for spinal cord injury repair

Jia Yang^{a,1}, Kunkoo Kim^{a,1}, Yaosai Liu^{b,1}, Xiaobin Luo^c, Chao Ma^b , Weitao Man^b, Yating Zhao^d, Zheng Cao^{a,e}, Peilun Hu^c, Junlin Chen^a , Yu Wang^f, Xiaodan Sun^a, Lingyun Zhao^a, Guihuai Wang^{b,**}, Kaiyuan Yang^{b,***}, Xiumei Wang^{a,*} 

^a State Key Laboratory of New Ceramics and Fine Processing, Key Laboratory of Advanced Materials, School of Materials Science and Engineering, Tsinghua University, Beijing, 100084, China

^b Department of Neurosurgery, Beijing Tsinghua Changgung Hospital, School of Clinical Medicine, Tsinghua University, Beijing, 102218, China

^c Department of Orthopedics, Beijing Tsinghua Changgung Hospital, School of Clinical Medicine, Tsinghua University, Beijing, 102218, China

^d Department of Neurology, Beijing Tsinghua Changgung Hospital, School of Clinical Medicine, Tsinghua University, Beijing, 102218, China

^e Center for Biomaterials and Regenerative Medicine, Wuzhen Laboratory, Tongxiang 314500, China

^f Department of Orthopedics, Peking University First Hospital, Beijing 100034, China

ARTICLE INFO

Keywords:

3D bioprinting
Dynamic bioink
Neural stem cells
Cell-instructive cues
Spinal cord injury

ABSTRACT

Biomimetic neural substitutes, constructed through the bottom-up assembly of cell-matrix modulus via 3D bioprinting, hold great promise for neural regeneration. However, achieving precise control over the fate of neural stem cells (NSCs) to ensure biological functionality remains challenging. Cell behaviors are closely linked to cellular dynamics and cell-matrix mechanotransduction within a 3D microenvironment. To address this, a dynamic bioactive bioink is designed to provide adaptable biomechanics and instructive biochemical cues, specifically tailored for the fate commitment of NSCs, through incorporating reversible Schiff-base bonds and bioactive motifs, N-cadherin-mimicking and BDNF-mimicking peptides. We demonstrate that the dynamic properties of 3D bioprinted living fibers alleviate the mechanical confinement on NSCs and significantly enhance their mechanosensing, spreading, migration, and matrix remodeling within the 3D matrix. Additionally, the inclusion of N-cadherin-mimicking and BDNF-mimicking peptides further enhances cells' ability to sense and respond to mechanical and neurotrophic cues provided by the surrounding matrix, which accelerates the self-organization of a functional neural network within the 3D bioprinted construct, leading to significant motor and sensory function recovery in a rat complete spinal cord injury model. This work underscores the critical role of precisely designing cell-instructive bioinks for the advanced functionality of 3D bioprinted living constructs in neural regeneration.

1. Introduction

Spinal cord injury (SCI) initiates a cascade of pathophysiological events that often lead to permanent neurological deficits, primarily due to limited endogenous regenerative motivations and continuous inhibitory microenvironment at the lesion site, particularly in cases of long-distance SCI [1]. Given that neural stem cells (NSCs) can differentiate

into distinct neural cell types to achieve cell supplement, as well as secrete neurotrophic factors to support neuronal activities, NSC transplantation has become a promising option for promoting SCI repair [2, 3]. However, the low survival rate and uncontrolled differentiation of transplanted NSCs in an inhospitable post-SCI niche extremely limit their therapeutic effects [4]. Hydrogels, acting as artificial extracellular matrix (ECM) that provide a customizable niche and mechanical support

* Corresponding author.

** Corresponding author.

*** Corresponding author.

E-mail addresses: guihuai_wang@163.com (G. Wang), yangky1992@126.com (K. Yang), wxm@mail.tsinghua.edu.cn (X. Wang).

¹ These authors contributed equally to the work.

for NSC survival and function, have emerged as superior candidates for therapeutic NSC delivery in biomedical applications [5–7]. Nevertheless, considering the complex biological characteristics of the natural spinal cord, it remains a formidable challenge to develop NSC-laden hydrogel grafts with biomimetic structures, diverse compositions, enhanced cell maturation, and reduced heterogeneity for precise SCI regeneration.

Three-dimensional (3D) bioprinting is an emerging technique with considerable potential to precisely control the spatial organization of various components such as stem cells, biomaterials, and bioactive molecules in a “bottom-up” manner [8–11]. As an additive manufacturing paradigm, 3D bioprinting holds great promise for the rapid fabrication of spinal cord analogs with architectural and componential complexity, enabling advances in SCI repair [12–14]. Our previous works have demonstrated that 3D bioprinting enables the construction of bioengineered living nerve fibers with high NSC capacity and oriented structural arrangement, providing directional guidance for the integration between renescent network and host tissue, thereby facilitating neural circuit reconstruction and in SCI rats [15]. Recently, evidence has shown that in living organisms, ECMs are microscopically dynamic and adaptable structures that undergo constant remodeling to accommodate the changing cellular needs [16]. Cellular behaviors including proliferation, migration, differentiation, and multicellular self-organization are critically dependent on the complex properties of the ECM [17,18]. Therefore, to create more biofunctional NSC-laden 3D bioprinting living constructs for SCI repair, it is crucial to design ECM mimetic bioinks that better replicate the dynamic biomechanical and biochemical properties of native stem cell niches.

One effective approach to address this issue is to develop structurally dynamic hydrogels with dynamic covalent bonds. Compared to traditional hydrogels with static networks, dynamic hydrogels demonstrate superiority in mimicking the dynamic structural, fast stress relaxation, and adaptive features of natural ECM [19]. Increasing evidence suggests that mechanical signals from the dynamic cellular niche make pivotal contributions to the commitment of stem cell fate [20,21]. Dynamic hydrogels can quickly relieve the stress generated by actin morphogenesis of encapsulated cells, enabling them to facilitate cell mechanotransduction, proliferation, migration, and differentiation. They also replicate the dynamic processes of cell-matrix and cell-cell interactions observed in native ECM [22]. Moreover, dynamic covalent bonds impart the shear-thinning and self-healing abilities to hydrogels, enhancing their printability and protecting encapsulated cells from shear forces during extrusion, making them ideal bioinks for 3D bioprinting [23]. However, dynamic covalent bonds can also render hydrogel susceptible to erosion and viscous flow over time, potentially leading to structural collapse and fragmentation after implantation. Recent studies have demonstrated that introducing additional covalent bonds, such as those activated by light-responsive curing, into the dynamic network can enhance both microscopic dynamics and macroscopic stability in synthetic hydrogels to address this challenge [24,25].

Notably, NSC fate commitment driven solely by dynamic mechanical signals presented by hydrogels is a gradual process that may not be sufficient to establish mature neural networks. In contrast to the highly sophisticated native ECM, structurally dynamic hydrogels still lack essential biochemical signals that directly modulate cell-hydrogel communications through specific ligand-receptor interactions, which could activate the particular downstream intracellular cascades, leading to a more efficient and targeted cell behavior guidance [26,27]. An ideal dynamic bioink system should recapitulate these intricate biochemical signals to provide cell-instructive cues. Key proteins, including cell adhesion molecules (CAMs) like N-cadherin and neurotrophic factors such as brain-derived neurotrophic factor (BDNF), are instrumental in constructing the biochemical signals of NSC niches [28,29]. Specifically, N-cadherin enhances NSC mechanotransduction by modulating cytoskeletal tension through actin filaments (F-actin), facilitating adhesion-mediated cell-matrix and cell-cell interactions that guide NSC

differentiation toward neuronal lineages [30,31]. Complementing this, BDNF establishes critical neurotrophic niches, further accelerating NSC differentiation into neurons and promoting synapse maturation [32]. Thus, co-delivering N-cadherin and BDNF in dynamic bioink could synergistically replicate the distinctive biochemical signals of the native NSC niche, promoting efficient neuronal differentiation and neural circuit maturation, thereby accelerating nerve repair [33]. However, the unstable complex hierarchical structure and low loading efficiency of the CAMs and soluble neurotrophic factors hinder their applications to a great extent [28]. The emergence of peptide biomimetics has introduced small molecular peptides as a promising alternative [34]. These small bioactive peptide sequences are designed to mimic the functionality of the native proteins, attaching to the hydrogel via dynamic covalent bonds that could replicate the dynamic biochemical cues of native ECM, directly stimulating cell development and responses [27,34–37].

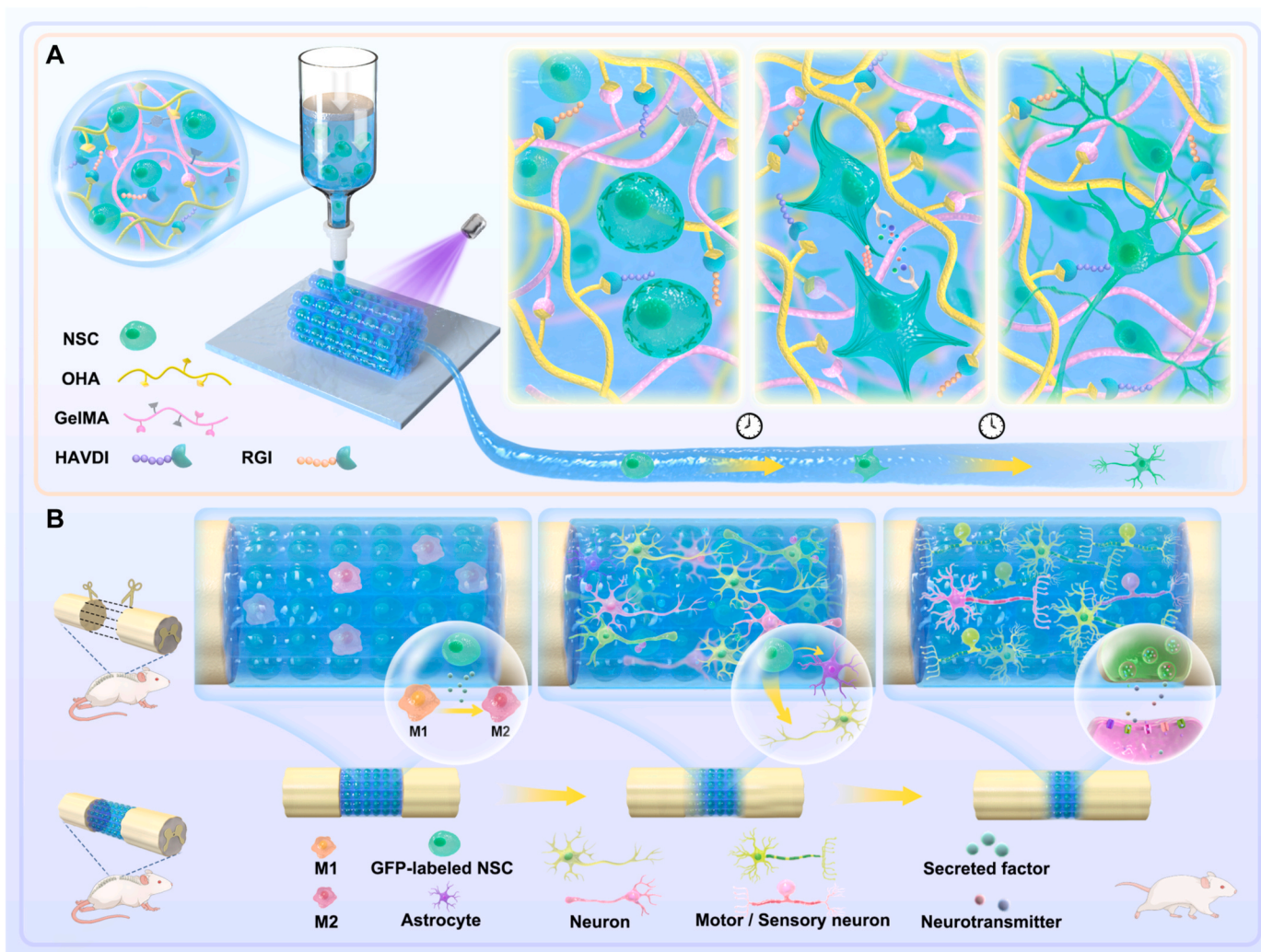
In this study, we explored an ECM mimetic bioink system based on methacrylated gelatin (GelMA)/oxidized hyaluronic acid (OHA) functionalized with bioactive peptides, carrying NSCs to construct a 3D bioprinted living microtissue with defined architecture of aligned fibers (referred to as GHP@NSC construct) for enhancing SCI repair (Scheme 1). The GHP bioink, formulated with Schiff-base bonding and peptide motifs, exhibits reinforced structural dynamicity, desirable bioprintability, and enhanced bioactivity. We also elucidated that the dynamic hydrogel network can provide a cell-adaptable microenvironment for the encapsulated NSC, and significantly enhanced cell-matrix mechanosensing within the 3D matrix. While the functionalization with bioactive motifs positively modulated mechanotransduction, neurotrophic secretion, and neuronal-oriented differentiation of NSCs *in vitro*. The therapeutic efficacy of the designed GHP@NSC microtissue was then evaluated in a rat spinal cord complete transection model. Our findings highlight that the orchestration of dynamic biomechanics and instructive biochemical cues in the GHP bioink significantly enhance cell-matrix and cell-cell interactions, facilitating mechanotransduction-assisted self-organization of the 3D bioprinted construct into a functional substitute with a developed neural network, and achieving remarkable motor and sensory function recovery in SCI rats.

2. Results and discussion

2.1. Synthesis and characterization of the designed hydrogels

In this study, we developed a dual-network dynamic bioink system using gelatin and hyaluronan (HA) to mimic the primary components of the natural ECM in the central nervous system. The initial dynamic network was formed through the Schiff-base reaction between the amino groups of GelMA and the aldehyde groups of OHA. This dynamic network of hydrogel presents structural dynamicity allowing for adaptable “cell-hydrogel” interactions, thereby facilitating cells’ mechanosensing [38]. To provide direct and effective bioactive signaling within this dynamic hydrogel network, we incorporated N-cadherin-mimetic peptide HAVDI and BDNF-mimetic peptide RGI via Schiff-base bonds with OHA, establishing a bioactive dynamic network. These peptides served as biochemical cues, presented as dynamic reversible bioligand, which mimics the ECM’s function to directly trigger intracellular signaling through cell surface receptors, further strengthening the transduction of “cell-hydrogel” interactions [39,40]. Additionally, to ensure the macroscopic stability of the hydrogel, a static covalent crosslinking network was formed between GelMA molecules (Fig. 1A).

We synthesized methacrylated gelatin (GelMA) and oxidized hyaluronic acid (OHA), which were confirmed by ^1H nuclear magnetic resonance (^1H NMR) spectra (Fig. S1, Supporting Information). The ^1H NMR spectrum confirmed the presence of characteristic methacrylate peaks at 5.4 ppm and 5.7 ppm in GelMA (Fig. S1A, Supporting Information) and aldehyde peaks at 4.83 ppm, 4.98 ppm, and 5.08 ppm in OHA (Fig. S1B, Supporting Information), with a modification degree of

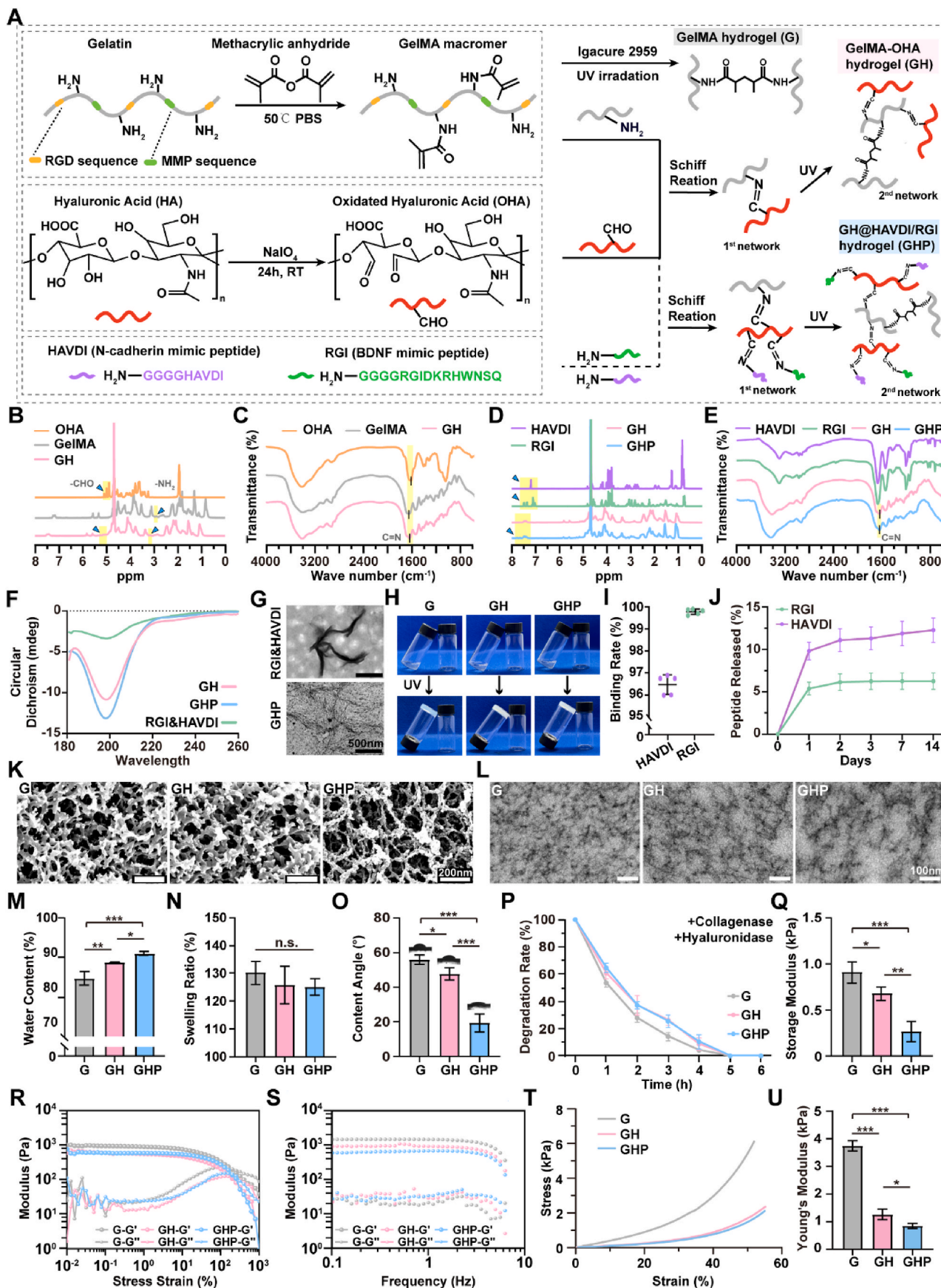


Scheme 1. 3D Bioprinted dynamic and bioactive living hydrogel modulates NSC fate commitment and enhances spinal cord injury repair. A) Schematic illustration of the GHP@NSC fabrication via 3D bioprinting and the development of the encapsulated NSCs induced by the dynamic biomechanics and biochemical cues. B) Schematic diagram of the regenerative mechanism of GHP@NSC construct in promoting SCI repair.

60 % for both. The GelMA and OHA were dissolved sufficiently to create a compound solution, referred to as GH prepolymer. The proton peak of the amino group in GelMA (2.9 ppm) and the peaks of the aldehyde group in OHA (4.83 ppm, 4.98 ppm, and 5.08 ppm) showed an obvious reduction in GH prepolymer as observed in the ^1H NMR spectrum (Fig. 1B). Meanwhile, the Fourier transform infrared spectroscopy (FTIR) spectrum revealed a shift in the absorption peak of C=N stretching vibration (Fig. 1C). These results indicated that GH prepolymers were conjugated via a Schiff-base reaction between the amino groups in GelMA and the aldehyde groups in OHA. Subsequently, HAVDI and RGI peptides were added to the GH prepolymer to obtain the GHP prepolymer. The ^1H NMR spectrum of the GHP prepolymer presented the proton peaks of tyrosine from HAVDI and tryptophan from RGI (Fig. 1D). Also, the GHP prepolymer showed a stronger absorption peak at 1637 cm^{-1} in comparison to the GH prepolymer in the FTIR spectrum (Fig. 1E). This result was ascribed to the stronger C=N stretching vibration resulting from Schiff-base conjugation of the peptides. The secondary conformation and microscopic structures of the peptides in GHP prepolymers were investigated by circular dichroism (CD) and transmission electron microscope (TEM). As shown in Fig. 1F, both RGI & HAVDI peptides and GH prepolymer exhibited typical β -sheet CD spectra with a negative band at 198 nm and a positive band at 182 nm, whereas the GHP prepolymer exhibited similar CD spectra with the

strongest negative band, demonstrating the preservation of β -sheet conformation of peptides in GHP prepolymers (Fig. 1F). In TEM images, RGI & HAVDI peptides exhibited a short nano-fibrous configuration, while a similar nano-fibrous micromorphology was observed in the GHP prepolymer, indicating that the microscopic structures of peptides remained intact in the GHP prepolymer (Fig. 1G).

After establishing the initial dynamic covalent crosslinking network among GelMA, OHA, and peptides through Schiff-base reaction, the hydrogels were obtained with further crosslinking under UV light to form a secondary static network (Fig. 1H). The binding and release behaviors of RGI and HAVDI peptides were investigated using mass spectrometry and high-performance liquid chromatography (HPLC). Both peptides exhibited relatively high binding rates and low release profiles after one day (Fig. 1I and J), indicating stable peptide conjugation within the hydrogel network. These results suggested that the bioactive motifs are more efficiently retained within the hydrogels, enhancing their modulation capability on encapsulated cells. Furthermore, scanning electron microscopy (SEM) and TEM images of G, GH, and GHP hydrogels showed a porous and nanofiber-like morphology (Fig. 1K and L), which could ensure the transportation of the nutrients and provide an ideal growth space for encapsulated cells. Additionally, the presence of peptides significantly elevated the water content and hydrophilicity of the hydrogel (Fig. 1M and O), indicating a more similar



(caption on next page)

Fig. 1. Synthesis and characterization of G, GH, and GHP hydrogels. A) Schematic illustration of the preparation and fabrication of G, GH, and GHP hydrogel. B) ^1H NMR spectra of GelMA, OHA, and GH. C) FTIR spectra of GelMA, OHA, and GH. D) ^1H NMR spectra of HAVDI, RGI, GH, and GHP. E) FTIR spectra of HAVDI, RGI, GH, and GHP. F) The CD spectra of GH prepolymer, GHP prepolymer, and the mixed solution of RGI & HAVDI peptides. G) The TEM images of the mixed solution of RGI & HAVDI peptides and GHP prepolymer. H) Macroscopic observation of UV-induced formation of G, GH, and GHP hydrogels. I, J) The binding rate (I) and the releasing rate (J) of RGI and HAVDI peptides on GHP hydrogel. K, L) The representative SEM (K) and TEM (L) images of the hydrogels. M – O) The water content (M), swelling ratio (N), and contact angle (O) of the hydrogels. P) The degradation behavior of the hydrogels. Q) The average storage modulus (G') of the hydrogels at 1 % strain and 1 Hz frequency. R, S) Rheological measurements of storage (G') and loss (G'') modulus of the hydrogels in a strain-sweep (R) and a frequency-sweep (S). T, U) Compression strain-stress curve (T) of the hydrogels and the compressive Young's modulus (U) of the hydrogels. Quantification data are represented as the mean \pm SD. * $P < 0.05$, ** $P < 0.01$, *** $P < 0.001$, n. s. No significant difference.

property to the native ECM. However, no significant differences were observed in swelling capacity among the three hydrogels (Fig. 1N), suggesting that the GHP hydrogel could maintain higher water content without excessive swelling expansion, making it a promising candidate for implant applications. Moreover, the *in vitro* enzymatic degradation experiment revealed that all three hydrogels were rapidly and fully degradable by collagenase and hyaluronidase (Fig. 1P), confirming their good biodegradability.

The biomechanical properties of hydrogels play a crucial role in guiding cell behaviors and nerve regeneration. The introduction of a dynamic covalent network significantly lowered the storage modulus of the hydrogels (Fig. 1Q), indicating softer and more nerve-like viscoelasticity properties in GHP hydrogel [41]. As shown in Fig. 1R and S, G, GH, and GHP hydrogels maintained relatively steady storage and loss modulus under the deformation ranging from 10^{-2} % to 10 % and frequencies from 0.1 Hz to 10 Hz. These results suggested that all three hydrogels exhibit rheological stability and may provide suitable structural support *in vivo*. Moreover, G hydrogel manifested a steeper strain-stress curve and a comparably much higher Young's modulus in compression evaluation compared to GH and GHP hydrogels, suggesting the dynamic covalent network could decrease the stiffness of the hydrogel to better suit the needs of neural cells development (Fig. 1T and U) [42].

2.2. Reinforced structural dynamicity, diffusive permeability, and desirable bioprintability of the GHP hydrogel

The reversible Schiff-base bonds endowed the hydrogel with dynamic characteristics, providing encapsulated cells with a dynamic adaptable microenvironment as a biomechanical cue to capture the intrinsic dynamic behavior of naive ECM (Fig. 2A). Owing to the dynamically reversible nature of the Schiff-base connections, the interface of separated GH and GHP hydrogel pieces showed obvious integration after 2 h of intimate contact, presenting a self-healing ability following the structural disruption (Fig. 2B). Besides, a continuous step-strain measurement was carried out. As shown in Fig. 2C, after 2 cycles from a low strain (1 %) to a high strain (500 %), the storage modulus (G') of GH and GHP hydrogel quickly and almost entirely returned to the initial value, whereas the G' of G hydrogel only reached 66 % of its initial value. This indicated that the dynamic network imparted a self-healing property to the GH and GHP hydrogel. Additionally, the dynamic reversible crosslinking chemistries of GH and GHP hydrogels exhibited progressively faster stress relaxation properties, with $\tau_{1/2}$ (the time for the initial stress to relax to half) being significantly shorter compared to the purely static crosslinking in G hydrogels (Fig. 2D and E), which contribute to relaxing cellular traction forces, thereby allowing for matrix remodeling [43].

The high permeability of the hydrogel network not only ensures rapid nutrient transport within the hydrogel but also facilitates efficient substance exchange with the surrounding environment, both of which are crucial for the regenerative potential of 3D bioprinted constructs [44,45]. However, larger complex growth factors (>30 kDa) related to NSC fate modulation may have difficulty diffusing and exchanging within the hydrogel network [2,46]. To assess the permeability of larger molecules in various hydrogels, we evaluated the loading and releasing behavior of fluorescein isothiocyanate (FITC)-conjugated bovine

albumin (BSA-FITC, 67 kDa) (Fig. 2F and H). As shown in Fig. 2G–J, the GHP hydrogel demonstrated a faster loading and releasing rate for FITC-BSA, along with a higher saturation concentration, indicating greater permeability compared to the GH and G hydrogel. This facilitated the efficient transportation of nutrients and metabolic waste in 3D bioprinted constructs.

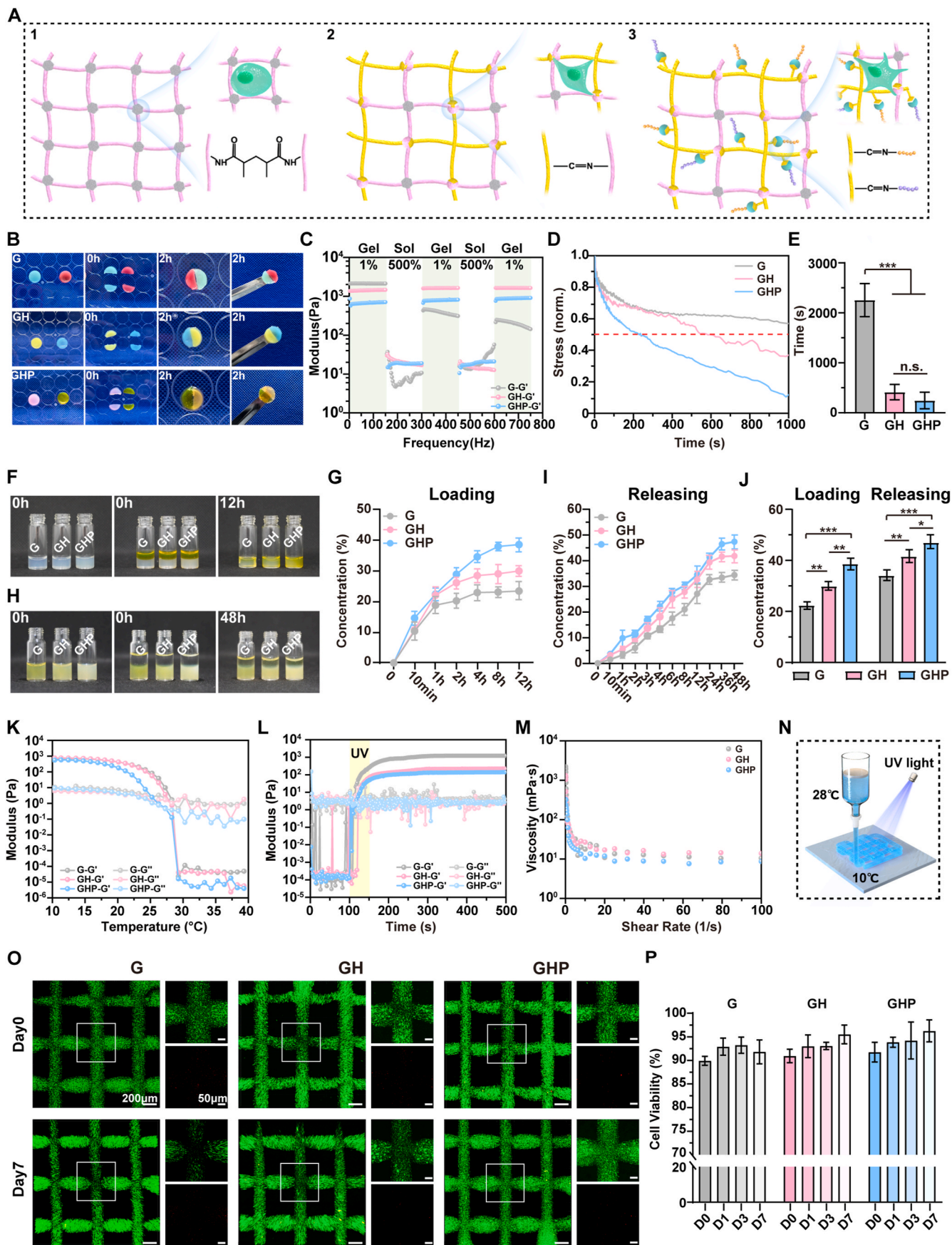
Owing to the thermo-sensitive cross-linking property of GelMA, the G, GH, and GHP solutions exhibited a similar gelation behavior ($G' = G''$) at approximately 28 °C (Fig. 2K). Upon UV light exposure, the G' values in the G, GH, and GHP solutions rapidly increased, surpassing G'' and eventually reaching saturation (Fig. 2L), indicating a gelation process. These results implied that introducing a dynamic covalent network into GelMA solutions had little impact on the thermo-sensitive and UV-sensitive crosslinking behavior of the hybrid solutions. Additionally, due to the dynamic nature of reversible bonds, the GH and GHP solutions exhibited more pronounced shear-thinning behavior, with viscosity drastically decreasing as the shear rate increased (Fig. 2M), which is beneficial in protecting cells from potential damage caused by shear force during the bioink extrusion process. Based on the rheological properties of the G, GH, and GHP solutions, we employed a two-step cross-linking strategy to achieve 3D bioprinting. The temperatures of the syringe and platform were set at 28 °C and 10 °C, respectively, enabling quick filament deposition through thermo-sensitive cross-linking, followed by UV light exposure for stable curing (Fig. 2N). Such a 3D bioprinting process preserves the hydrogel's chemical structure and mechanical properties, while the layer-by-layer stacking manner ensures the overall structural integrity of the 3D printed constructs.

Subsequently, to investigate the bio-printability of G, GH, and GHP solutions, the NSC-laden bioink was prepared using isolated NSCs from the hippocampus of embryonic SD rats (Fig. S2, Supporting Information) mixed with each respective hydrogel solution and printed to form a framework construction. As illustrated in Fig. 2O, the G, GH, and GHP bioinks exhibited excellent printability, achieving a high-precision and stable grid structure. Moreover, the majority of cells encapsulated within the G, GH, and GHP constructs exhibited high viability (>90 %) after 3D bioprinting (Fig. 2P), indicating that the relatively gentle printing process had a minor impact on cell viability. Notably, after 7 days of *in vitro* culture, the viability of NSCs within the GHP construct reached 96.26 ± 2.33 %, higher than that within the GH (95.52 ± 1.97 %) and G (91.83 ± 2.54 %) constructs (Fig. 2P). This result suggested that the dynamic biomechanics and biochemical cues of the bioink contribute to the maintenance of high cell viability within the encapsulated NSCs in a 3D bioprinted construct.

2.3. Enhanced mechanotransduction, neurotrophic secretion, and neuronal differentiation of NSCs in the GHP hydrogel

To enhance the cell-instructive capacity of dynamic bioink, HAVDI and RGI peptides were incorporated in the GHP bioink, serving as function-encoding biochemical cues to modulate special cell-hydrogel interactions, and thereby directly control NSCs mechanotransduction, neurotrophic secretion, and neuronal differentiation (Fig. 3A).

We first assessed the expression levels of mechanotransduction-related genes in NSCs encapsulated by G, GH, and GHP hydrogels. After 3 and 7 days of culture in differentiation medium, the GH group presented upregulated expression of protein kinase B (AKT), mitogen-



(caption on next page)

Fig. 2. Dynamicity and printability evaluation of G, GH, and GHP hydrogel. A) Schematic illustration of static, dynamic, and dynamic bioactive hydrogel networks in G, GH, and GHP hydrogels. B) Macroscopic self-healing behavior of the hydrogels. C) The damage-healing property of the hydrogels under low-high strain (1%–500%). D, E) The rheological stress-relaxation property (D) and the average half-time (E) of the hydrogels. F–J) The demonstration of FITC-BSA loading (F) and releasing (H) capability of the hydrogels, the loading (G) and releasing (I) rate of FITC-BSA in corresponding hydrogels, and the average FITC-BSA equilibrium concentration (J) of loading and releasing assessment in the hydrogels. K–M) The temperature-dependent gelation behaviors (K), UV sensitivity (L), and the shear-thinning properties (M) of the G, GH, and GHP prepolymers. N) The schematic diagram of the 3D bioprinting process. O) Representative Live (green)/Dead (red) staining images of 3D bioprinted NSC-laden G, GH, and GHP constructs cultured for 0 and 7 days. P) Cell viability (%) of 3D bioprinted NSC-laden G, GH, and GHP constructs at Day 0, Day 1, Day 3, and Day 7 cultivation. Cell viability (%) is calculated by dividing the number of live cells by the total number of cells at each corresponding time point. Quantification data represent mean \pm SD. * $P < 0.05$, ** $P < 0.01$, *** $P < 0.001$, n. s. No significant.

activated protein kinase (MAPK), Actin, β -catenin, yes-associated protein (YAP), Vinculin, N-cadherin, and neurogenic locus notch homolog protein 1 (Notch1) genes, compared to NSCs in the G hydrogels, whereas the GHP group exhibited the highest expression levels (Fig. 3B). Moreover, as shown in Fig. 3C and D, after 7 days of culture, the NSCs encapsulated by the GHP hydrogel exhibited significantly increasing nuclear translocation of YAP (a mechanosensing transcription factor), compared to those in G ($P < 0.001$) and GH ($P < 0.01$) hydrogels. These findings indicate that the dynamic characteristics of the hydrogel network significantly enhanced NSCs' mechanosensing to the matrix. Additionally, incorporating the HAVDI and RGI peptides into this dynamic network amplified NSC mechanotransduction by providing essential ECM biochemical cues through dynamic bioligand presentation [40]. Notably, the distinct presentation modes of the HAVDI peptide within the hydrogel might impact the mechanotransduction ability of encapsulated NSCs differently, while ultimately guiding them toward a consistent fate commitment to neurogenesis [47].

We then evaluated the mechanotransduction-dependent morphogenesis of NSCs encapsulated in the G, GH, and GHP hydrogels. The NSCs encapsulated in dynamic hydrogel demonstrated a significantly lower degree of cell sphericity compared to the static hydrogel group (Fig. 3E). Further, visualization of SEM and F-actin immunostaining revealed that NSCs in the G hydrogel with a static structure network presented a nearly initial round morphology after 7 days of culture. In stark contrast, NSCs in the GH and especially in the GHP hydrogel showed more remarkable extending protrusions and noticeable spreading (Fig. 3F and G). Notably, the NSCs within the GHP hydrogel significantly self-organized into an interconnected cellular network after 14 days of culture, in comparison to those in the G and GH hydrogels (Fig. 3H). This indicated a rapid cell-cell network assembly driven by the biomechanical and bioactive signals of the GHP hydrogel, which is of great importance for promoting the development of 3D bioprinted living microtissues [6,20].

To investigate the impact of the dynamic biomechanical and tailored biochemical signals presented by the hydrogels on NSC secretion behavior, we prepared 3D bioprinted living constructs using G, GH, and GHP bioinks, and cultured them in a proliferative medium. Fig. 3I illustrated that, compared to NSC in G and GH hydrogels, the expression levels of cytokine-related genes such as brain-derived neurotrophic factor (BDNF), nerve growth factor (NGF), neurotrophin-3 (NT-3), ciliary neurotrophic factor (CNTF), glial cell line-derived neurotrophic factor (GDNF), vascular endothelial growth factor (VEGF), platelet-derived growth factor (PDGF), and fibroblast growth factor (FGF) were highest in the GHP hydrogel after 1, 3, and 7 days of culture, with significant differences observed. Additionally, NSCs in the GH group showed notably increased gene expression levels of these growth factors compared to NSCs in the G group. Subsequently, in the Enzyme-Linked Immunosorbent Assay (ELISA), similar results were observed. The NSCs in the GHP hydrogel showed the highest secreted levels of the typical neurotrophins, including BDNF, NGF, NT-3, and CNTF, which are especially necessary for neural system development (Fig. 3J–M). Collectively, an adaptable microenvironment provided by the dynamic hydrogel network granted NSCs a stable and continuously enhanced capacity for nutritional factors secretion. The biochemical cues, dynamically integrated within the hydrogel, further amplified NSCs' secretory potential. Notably, owing to the efficient secretion ability of

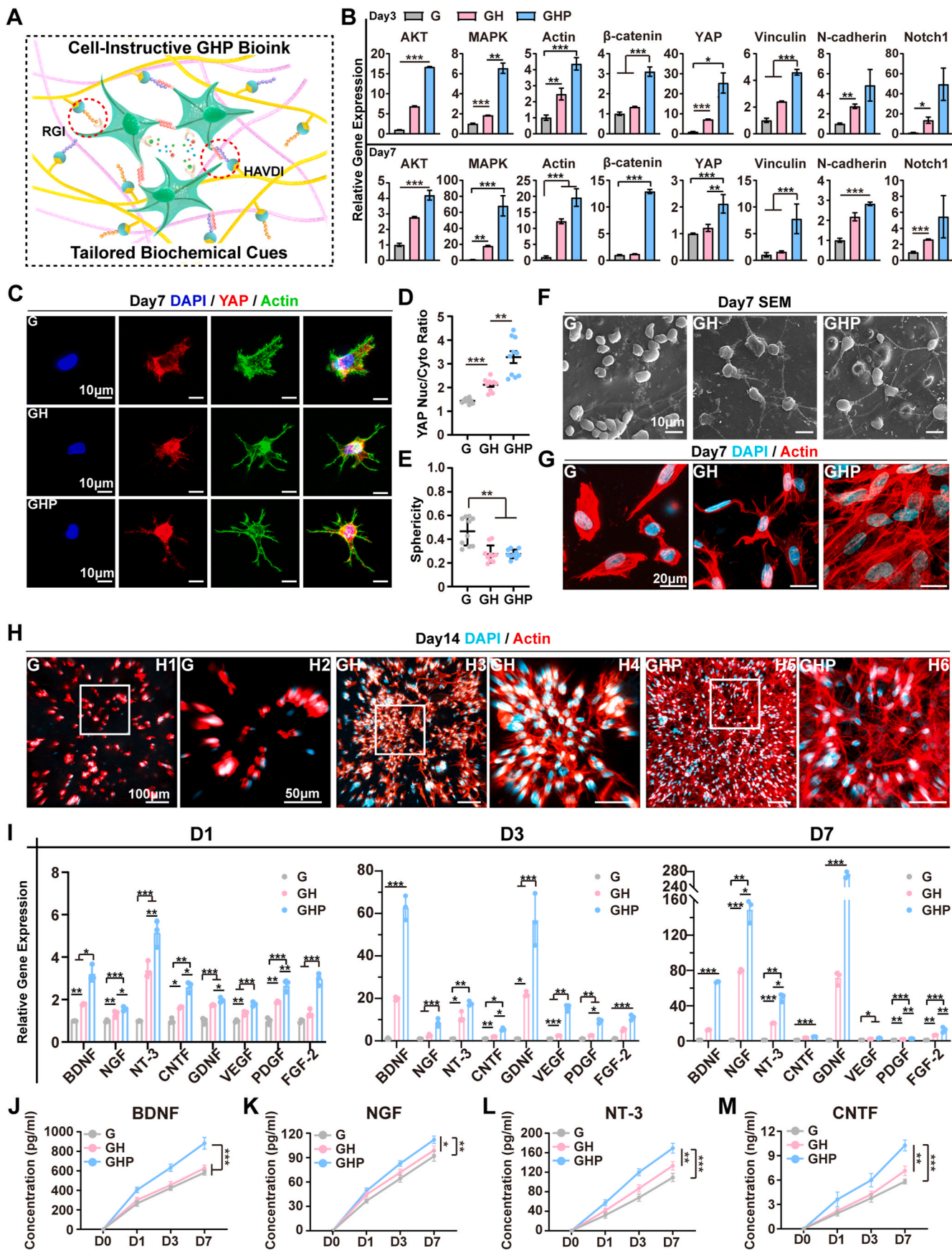
encapsulated NSCs, the 3D bioprinted constructs could operate as a dynamic, embodying the concept of a true "living biomaterial" [48].

To examine the differentiation behavior of the encapsulated NSCs within 3D bioprinted constructs, the gene and protein expression levels were analyzed. After 3 days of culturing in a differentiation-inducing medium, the relative expression levels of the stemness-related gene, including Nestin, sex determining region Y-box 2 (Sox 2), and Kiel 67 (Ki67), were significantly downregulated in the GHP group compared to the G and GH group (Fig. S3, Supporting Information). Moreover, the NSCs encapsulated in the GHP hydrogel showed significantly higher expression levels of the neuron-related genes such as β -tubulin III, and microtubule-associated protein 2 (MAP2), and lower expression levels of the astrocyte-specific genes glial fibrillary acidic protein (GFAP), compared to other hydrogels, after 3 days and 7 days of culture. These results indicated that the GHP hydrogel can accelerate the differentiation of encapsulated NSCs into neurons. Meanwhile, it is worth noting that after only 7 days of culture, NSCs in the GHP hydrogel showed remarkably higher expression levels of the synapse-specific genes synapse (SYN) and postsynaptic density protein 95 (PSD95). Next, the immunostaining was carried out using β -tubulin III and GFAP antibodies to further visualize and quantify. It was obvious that β -tubulin III-positive neurons extended and connected within the 3D bioprinted construct fabricated using GHP bioink (Fig. S4A, Supporting Information). Moreover, consistent with the gene expression results, the NSCs in the GHP hydrogel showed the highest neuronal and lowest astrocyte differentiation ratios compared to the G and GH groups (Figs. S4B and C, Supporting Information). We then detected the neural network formation within the 3D bioprinted construct through immunostaining for the mature neuron marker MAP2, and the synapse-specific marker SYN. As shown in Fig. S5 (Supporting Information), synaptic connections appeared among the MAP2-positive neurons in the GH and GHP hydrogels, which could not be observed in the G hydrogel.

Collectively, the above results confirmed that the dynamically adaptable microenvironment enhanced NSCs' mechanosensing and cell-force-induced morphogenesis, providing essential support for NSC-driven self-organization within the 3D matrix. Notably, while upon the cell-instructive biochemical cues involved, it showed great effects on the NSCs' mechanotransduction, neurotrophic secretion, and neuron-oriented differentiation.

2.4. The underlying mechanism in the NSC fate commitment modulated by the dynamic biomechanics and biochemical cues of hydrogels

To elucidate the underlying mechanisms modulating the fate of encapsulated NSCs with different bioinks, RNA sequencing analysis was conducted on G@NSC, GH@NSC, and GHP@NSC constructs after 14 days of cultivation. As shown in Fig. 4A, the expression profiles exhibited marked differences between GH vs. G and GHP vs. GH, with 2055 and 2120 genes upregulated in the respective comparison groups. Notably, among the total differentially expressed genes (DEGs) in GH vs. G and GHP vs. GH, 1653 genes were shared by both comparison groups. However, only 131 genes were common among the upregulated DEGs (Fig. 4B), suggesting that distinct mechanisms might be involved in the fate commitment of the encapsulated NSCs, driven by biomechanical cues from structural dynamicity and biochemical cues from bioactive motifs.



(caption on next page)

Fig. 3. Mechanotransduction and secretion profile of NSCs encapsulated in 3D bioprinted G, GH, and GHP constructs *in vitro*. A) Illustration of HAVDI and RGI peptides function in GHP@NSC 3D bioprinted constructs. B) Relative gene expression of NSCs mechanical signaling related genes in G@NSC, GH@NSC, and GHP@NSC 3D bioprinted constructs at Day 3 and Day 7 cultivation. C) Representative images of 3D bioprinted constructs cultured for 7 days immunostained with DAPI (blue), YAP (red), and Actin (green). D) Quantitative analysis of the YAP fluorescence intensity ratio between the nucleus and cytoplasm; $n = 10$. E) The sphericity quantification of the NSCs encapsulated in the 3D bioprinted constructs; $n = 10$. F) SEM images of NSCs in 3D bioprinted constructs cultured for 7 days. G, H) Cytoskeleton staining images of 3D bioprinted constructs at Day 7 (G) and Day 14 (H) cultivation. H2, H4, and H6 are enlarged views of marked area in H1, H3, and H5, stained with phalloidin (red) and DAPI (blue). I) Relative gene expression of NSCs secretion-related genes in 3D bioprinted constructs at Day 1, Day 3, and Day 7 cultivation. J–M) The neurotrophins BDNF (J), NGF (K), NT-3 (L), and CNTF (M) secretion of NSCs in 3D bioprinted constructs at Day 1, Day 3, and Day 7 cultivation. Quantification data represent mean \pm SD. * $P < 0.05$, ** $P < 0.01$, *** $P < 0.001$, n. s. No significant difference.

To clarify the separate impacts of biomechanical and biochemical cues on NSC behaviors, the upregulated genes in GH vs. G and GHP vs. GH were enriched and analyzed using Gene Ontology (GO) biological process analysis respectively (Fig. 4C and D). In the GH vs. G group, the upregulated genes were significantly enriched in “extracellular matrix organization”, “cell adhesion mediated by integrin”, “cell-matrix adhesion”, and “integrin-mediated signaling pathway” (Fig. 4C), suggesting that the dynamic biomechanics in adaptable networks prominently enhanced the mechanosensitivity of encapsulated NSCs, leading to more active cell-ECM interactions, including cell adhesion, migration, mechanotransduction, and ECM remodeling. Meanwhile, the upregulated DEGs in GHP were significantly enriched in “nervous system development”, “homophilic cell adhesion via plasma membrane adhesion molecules”, “chemical synaptic transmission”, “cell adhesion”, “synapse organization”, and “neuron differentiation” (Fig. 4D). This result indicated that NSCs encapsulated in the GHP hydrogel exhibited enhanced cellular adhesion and facilitated the formation of complex synaptic connections, demonstrating that the bioactive motifs effectively induced cell-cell interactions and promoted neural network formation. Specifically, the introduction of HAVDI reinforced cell-cell adhesion and direct transduction of neurogenesis-related signals [28, 49], while the addition of RGI could have accelerated neuronal maturation and synapse formation [50,51], synergistically contributing to the functional neural network establishment within the GHP construct. Then, we investigated pivotal genes and crucial signaling pathways within the selected GO terms (highlighted in Fig. 4C and D) to further reveal the mechanisms underlying the roles of adaptable mechanics and refined biochemical cues in NSC fate commitment.

First, to select pivotal genes in GH vs. G and GHP vs. GH comparison groups, we conducted string interaction network analysis on all enriched genes involved in the selected GO terms, identifying 140 genes in GH vs. G and 366 genes in GHP vs. GH, respectively (Figs. S6 and S7, Supporting Information). Subsequently, the top 10 % of genes with the highest number of node connections were chosen for heatmap analysis and their corresponding protein-protein interaction (PPI) network mapping (14 genes for GH vs. G and 37 genes for GHP vs. GH). The heatmaps of these selected genes illustrated apparent differences in expression levels (Fig. 4E and G), while forming intricate interlocking connections in the PPI networks as well (Fig. 4F and H). Notably, the selected genes in GH vs. G comparison groups were mainly related to cell adhesion molecules (Itga1, Itga2, Itga4, Itga8, Itgb1, Itgb8, and Postn) and ECM components (Fbn1, Fn1, Col1a2, and Col3a1) (Fig. 4E and F). This indicated that the dynamic characteristics in GH enhance cell-matrix interactions by increasing NSCs’ sensitivity to the mechanical signals from the surrounding matrix through integrin activation and capacity of ECM remodeling via secretion. Additionally, the selected genes in the GHP vs. GH comparison group were mostly associated with neuronal differentiation (Pax 6, Neurog1, Lrrtm4, Notch1, Erbb3, Erbb4, Olfm1, etc.), Cadherin expression (Cdh1, Cdh2, Ctnna2, and Ctbnnd2), neurotransmitter receptor activation (Grin2b, Gria2, Gria4, Grink1, Grin1, Grid 2, Htra3a, etc.), and synapse formation (Syn 1, Snap 25, Gabra2, Grm5, Gad 2, etc.). The upregulation of Cadherins and differentiation-related gene expression was facilitated by the introduction of bioactive motifs, showing significantly increased cell-cell interactions. This modulation accelerated neuronal development and the establishment of functional neural networks, as evidenced by the activation of various

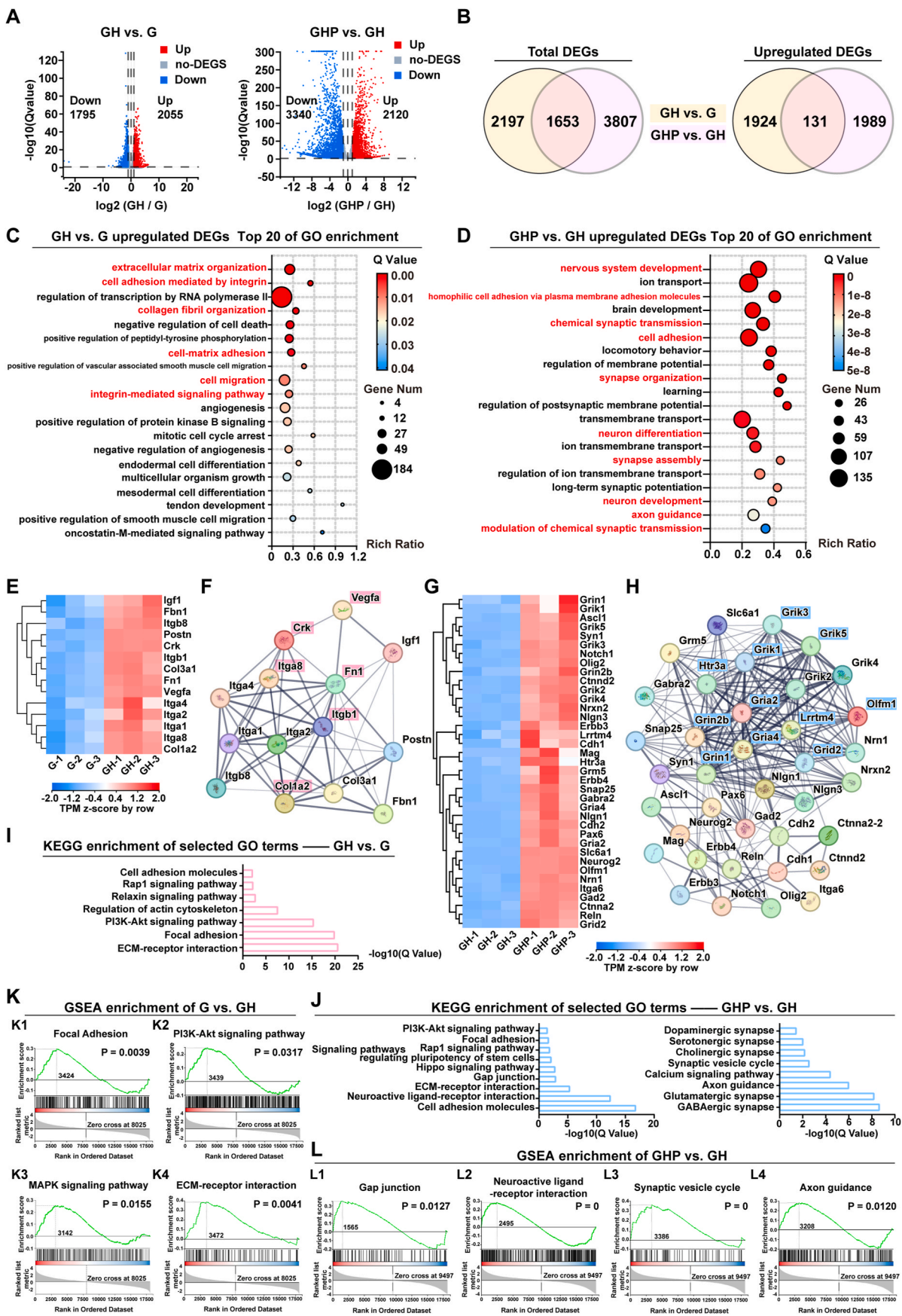
synapse and neurotransmitter receptor proteins. The quantitative real-time polymerase chain reaction (qRT-PCR) result confirmed that the top 3 % of key genes were significantly upregulated at the mRNA level (Fig. S8, Supporting Information).

Next, the related DEGs involved in the selected GO terms were further analyzed using the Kyoto Encyclopedia of Genes and Genomes (KEGG) enrichment bar plots. In the GH vs. G comparison groups, the selected upregulated DEGs were significantly enriched in “ECM-receptor interactions”, “Focal adhesion”, “PI3K-AKT signaling pathway”, and “Regulation of actin cytoskeleton” (Fig. 4I). The gene set enrichment analysis (GSEA) results also revealed significant upregulation of these signaling pathways in the GH construct (Fig. 4K). These results revealed that the structural dynamicity of the hydrogel could trigger mechanosensing and mechanotransduction pathways (ECM-receptor interactions, PI3K-AKT signaling pathway, Focal adhesion, and MAPK signaling pathway) in the encapsulated NSCs, further modulating molecular pathways related to cell adhesion, migration, and morphogenesis (Cell adhesion molecules, Rap 1 signaling pathway, and Regulation of actin cytoskeleton). Meanwhile, in the GHP vs. GH comparison group, the enriched KEGG pathways could be divided into two categories: pathways involved in cell-cell or cell-matrix interactions (cell adhesion molecules, neuroactive ligand-receptor interaction, ECM-receptor interaction, and gap junction) and pathways involved in neuroactive development (GABAergic synapse, glutamatergic synapse, axon guidance, and calcium signaling pathway) (Fig. 4J). These results might explain the mechanisms underlying the functions of the two bioactive peptides: RGI might guide NSC behaviors by providing persistently stable neurotrophic supplement and triggering pathways like “Neuroactive ligand-receptor interaction” or “Signaling pathways regulating pluripotency of stem cells”, while HAVDI may reinforce intercellular interactions through “Gap junction”, as well as magnify the role of the dynamicity via “ECM-receptor interactions”. Pathways associated with neuronal functioning (Axon guidance and Calcium signaling pathways) and profuse synapse formation (synaptic vesicle cycle and multifarious synapses) could be activated by the synergistic modulation of RGI and HAVDI. The GSEA results also verified that these key pathways were significantly upregulated in GHP (Fig. 4L).

Our findings highlight the importance of orchestrating dynamicity and bioactivity cues to magnify the cell-matrix and cell-cell interactions, thereby facilitating the functional development of a self-organized neural network within the 3D bioprinted construct. Consequently, GHP@NSC could be considered a promising 3D-bioprinted living construct for spinal cord injury repair.

2.5. GHP@NSC promoted motor and sensory functional recovery in SCI rats

Given that the GHP@NSC construct demonstrated the highest capacity for NSC-driven functional neural network formation *in vitro*, we selected GHP@NSC for *in vivo* studies to further investigate its regenerative effects on spinal cord injury repair. To trace the fate of exogenous NSCs and their participation in the nerve regeneration process, we successfully labeled NSCs with green fluorescent protein (GFP) beforehand (Fig. S9, Supporting Information). Subsequently, a rat 4-mm complete spinal cord transection injury model at T9-T10 was established (Fig. S10, Supporting Information). GHP@NSC and GHP



(caption on next page)

Fig. 4. The mechanism underlying the fate commitment of NSC in 3D bioprinted constructs based on RNA sequencing. A) Volcano plots of transcriptomic analyzed differentially expressed genes (DEGs) in GH vs G (GH@NSC compared with G@NSC as control), and GHP vs GH (GHP@NSC compared with GH@NSC as control). B) The Venn diagram of the numbers of total and up-regulated DEGs in different comparison groups. C, D) Top 20 enriched terms in GO-P (Gene Ontology-biological process) enrichment analysis for up-regulated DEGs between GH vs G (C), and GHP vs GH (D). E-H) Heatmaps of the top 10 % pivotal genes involved in selected GO terms in GH vs G (E) and GHP vs GH (G), and the String protein-protein interaction networks of the selected genes of GH vs G (F) and GHP vs GH (H). I, J) The bar plots of enriched KEGG (Kyoto Encyclopedia of Genes and Genomes) pathways involved in the selected GO terms in GH vs G (I) and GHP vs GH (J). K, L) GSEA analysis of pivotal KEGG pathways in GH vs G (K) and GHP vs GH (L) respectively. RNA sequencing analysis was conducted in a two-sided comparison with biological independent triplicate (n = 3).

constructs were transplanted and kept for 12 weeks, while the Blank control group was treated with saline injection (Fig. 5A).

We examined the hindlimb locomotion performance in the SCI rats using Basso, Beattie, Bresnahan (BBB) scores on a weekly basis in a double-blind manner. The mean BBB score in the GHP@NSC group increased steadily. At 12 weeks post-SCI, the BBB scores of rats in the GHP@NSC group were significantly higher than those in the other groups (Fig. 5B). Moreover, rats treated with GHP@NSC hydrogel showed distinct motor function recovery, as evaluated by Catwalk footprints analysis. The rats in the GHP@NSC group exhibited more pronounced weight-bearing steps and toe spreading of hind paws (Fig. 5C and D), along with occasional forelimb-hindlimb coordination (Fig. 5D). In contrast, the hindlimbs of those rats in the GHP and Blank groups moved with little to no weight support. Furthermore, the hot plate test and Von Frey test were used to determine the recovery of sensory functions after SCI (Fig. 5E and F). Treatment with GHP@NSC hydrogel significantly enhanced heat sensitivity in the hot plate test and mechanical nociception in the Von Frey test, indicating improved sensory perception recovery.

The restoration of neural relay at the lesion site was also evaluated by electrophysiological analysis (Fig. 5G and H). At 12 weeks post-surgery, no discernible motor evoked potential (MEP) or sensory evoked potential (SEP) signals were detected in the Blank group. Treatments with GHP and GHP@NSC hydrogels both significantly increased the amplitude and shortened the latency of MEP and SEP signals. The effects of the GHP@NSC hydrogel were particularly prominent, although the amplitude and latency had not yet recovered to normal levels. These results demonstrate that in the GHP@NSC group, the reconstructed neural circuit effectively accelerated the transmission of electrical signals across the lesion center.

We then evaluated the potential of GHP@NSC hydrogel implantation to promote tissue repair in the injured spinal cord and malfunctioned bladder. As shown in Fig. 5I, the lesion epicenters in the Blank samples were nearly devoid of tissue. The newly regenerated tissues in the GHP group partially filled the lesion, with some irregular cavities, whereas those in the GHP@NSC group were more seamlessly integrated with the host spinal cord tissues. As expected, we found that the axial T1-weighted magnetic resonance imaging (MRI) signals in the GHP@NSC group showed a marked increase in the central isointense region, showing a more similar intensity to the normal spinal cord in comparison to the Blank group and GHP group. These *in vivo* image-logical evidences indicated the implantation of GHP@NSC had achieved better histological recovery of spinal cord tissue.

Neurogenic bladder is a common and serious complication of SCI, potentially leading to urinary infection, renal failure, and even life-threatening conditions [52]. To investigate the relationship between SCI and pathological changes in the bladder, we examined the microscopic pathological characteristics of bladders in each group with hematoxylin and eosin (H&E) staining and Masson staining (Fig. 5K). In the Blank group, fibrosis and muscle atrophy of the bladder wall were observed, whereas these abnormalities were remarkably alleviated by the treatment of GHP@NSC implantation. Our results validated the beneficial effects of GHP@NSC hydrogel in bladder protection post-SCI, which is also a major indicator of nerve repair. Additionally, no marked pathological changes were observed in major organs including the heart, liver, lungs, spleen, and kidneys, across various groups (Fig. 5L), indicating the reliable *in vivo* biosafety of the GHP@NSC hydrogel and its

promising potential for broader biomedical applications.

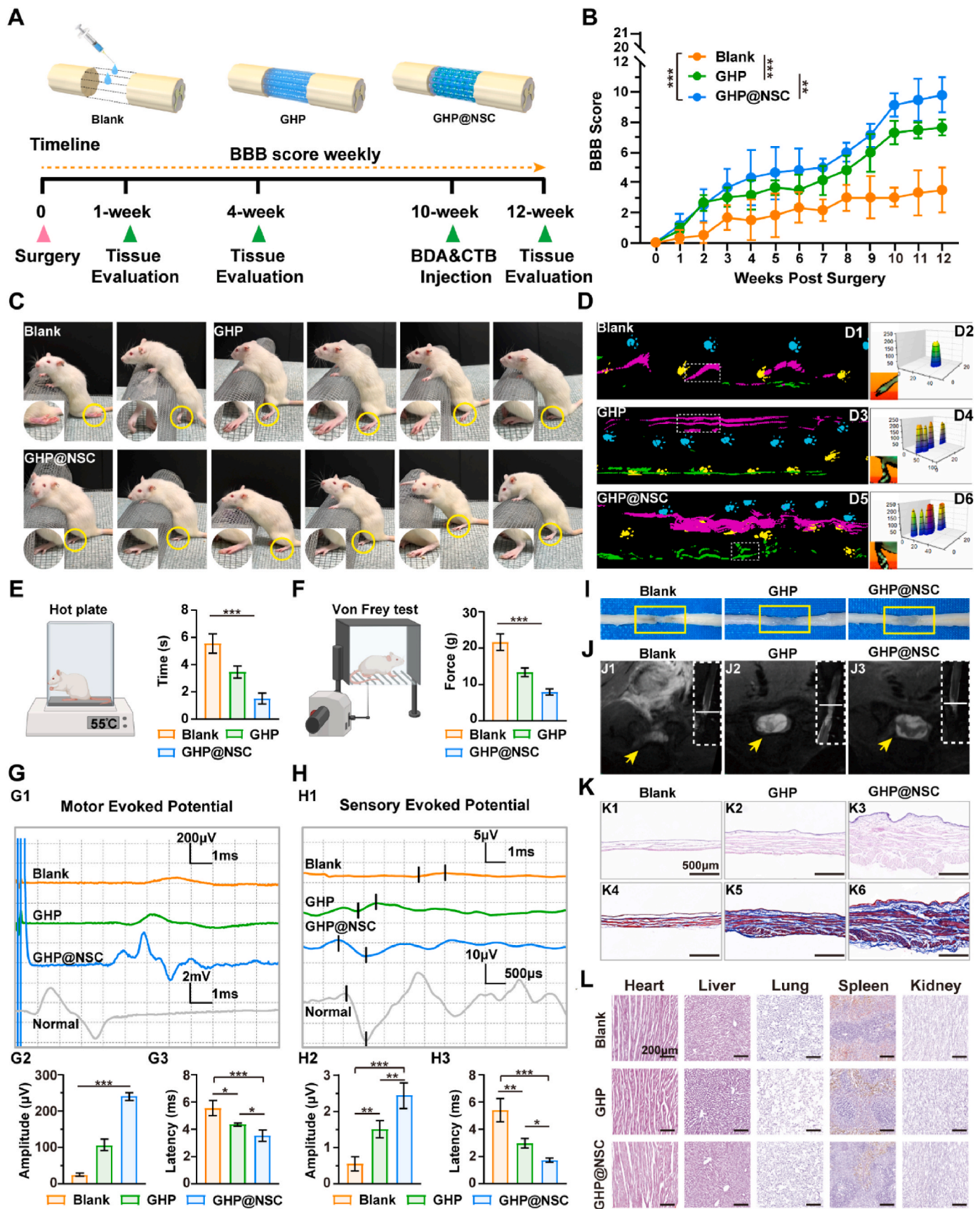
2.6. Regulation on neuroinflammatory microenvironment by GHP@NSC

A major challenge in repairing SCI is the complicated neuroinflammatory microenvironment at the lesion site that hinders nerve regeneration [53–55]. Clear evidence has shown that NSCs can act as receptors and regulators of neuroinflammation, and their cellular secretome plays a key role in apoptosis and immune regulation [56,57]. However, immunostimulatory macrophages are rapidly recruited, activated, and polarized to induce inflammatory storms that peak within 7 days after acute SCI, which extremely limits the survival and efficacy of implanted NSCs [58]. Thus, upgrading the NSC-delivery hydrogel with more natural ECM properties could be an effective way to achieve long-term encapsulated NSC development and modulate inflammatory responses by altering macrophage behavior.

To investigate the effect of GHP@NSC on modulating the inflammation microenvironment, we first used a transwell coculture system *in vitro*. In this setup, HAPI rat microglial cells were activated by adding lipopolysaccharide (LPS)/Interferon- γ (IFN- γ) and co-cultured with GHP@NSC hydrogel (Fig. 6A). The expression of inflammation-related genes in HAPI cells was measured by qRT-PCR after 24 h of coculture. Statistical analysis of qRT-PCR showed that the pro-inflammatory genes (Arginase-1 (Arg-1), found in inflammatory zone proteins (Fizz), chitinase-like 3 (YM-1), CD206, Interleukin-10 (IL-10), Interleukin-4 (IL-4)) were significantly suppressed in the GHP@NSC group, while the anti-inflammatory genes (inducible nitric oxide synthase (iNOS), tumor necrosis factor- α (TNF- α), CD86, Interleukin-6 (IL-6), Interleukin-1 β (IL-1 β), Interleukin-12 (IL-12)) were remarkably upregulated compared to other groups (Fig. 6B). The results manifested that the GHP@NSC hydrogel could polarize M2 microglia (anti-inflammatory phenotype) while inhibiting M1 microglia (pro-inflammatory phenotype), thereby exerting a regulatory biological effect on immune response during the initial stages of inflammation *in vitro*.

We further evaluated macrophages at the lesion site 7 days after SCI by immunofluorescence staining. Fig. 6C showed an abundant aggregation of CD68⁺ (a marker of activated macrophages) cells at the lesion epicenter in the untreated Blank group. In contrast, treatment with GHP@NSC hydrogel markedly reduced the number of CD68⁺ macrophages and facilitated the polarization of M2 macrophages (CD68⁺ cells also co-expressed CD206) compared to the other groups (Fig. 6C–E). In the meantime, qRT-PCR also demonstrated that the GHP@NSC hydrogel inhibited inflammation more effectively compared to the GHP hydrogel and Blank groups (Fig. 6F). Moreover, both GHP and GHP@NSC treatments significantly downregulated the expression of pro-apoptosis genes (Bcl-2-associated X protein (Bax), Interleukin-1 α (IL-1 α), Caspase-3 (Cas3), Caspase-9 (Cas9)) while boosting the level of anti-apoptosis gene Bcl-2 compared to the Blank group (Fig. 6G). Notably, the expression of senescence genes including p53, p21, and p16 was also significantly attenuated by GHP@NSC hydrogel treatment (Fig. 6H). These results are consistent with previous *in vitro* studies, indicating that GHP@NSC hydrogel plays a critical role in creating a favorable immunological microenvironment for nerve regeneration in the early stage after SCI, including alleviating the inflammatory storm, modulating the polarization of activated macrophages to the M2 phenotype, and suppressing cellular apoptosis and senescence at the injury site.

Previous research showed that an acute inflammatory storm can



(caption on next page)

Fig. 5. Functional recovery evaluation 12 weeks after SCI. A) Schematic illustration of animal experiment grouping and evaluation timeline *in vivo*. B) The BBB scores of rats in Blank, GHP, and GHP@NSC groups each week post-surgery. Two-way repeated measures analysis of variance (ANOVA) was applied, and * $P < 0.05$, ** $P < 0.01$, *** $P < 0.001$. C) Representative photographs of rats' hindlimbs and weight-bearing of rats in different groups. D) Representative walking gaits (D1, D3, D5) and the detailed footprints (D2, D4, D6) of rats recorded by Catwalk system. E) Illustration and average threshold time in the temperature allodynia experiments. F) Illustration and average threshold force in the mechanical allodynia experiment. G, H) Representative individual electrophysiological traces and quantitative analysis of average amplitude and latency in MEP (G) and SEP (H). I) Representative photographs of spinal cord specimens of different groups of rats; the yellow rectangles indicate the lesion sites. J) Representative images of T1-weighted MRI imaging; the dotted rectangles indicate coronal sections for lesion localization; the horizontal lines indicate the approximate position of the axial slice. K) Representative images of H&E and Masson staining of bladder tissues in different groups of rats. L) H&E staining images of hearts, livers, lungs, spleens, and kidneys sections in different groups of rats. Quantification data represent mean \pm SD. * $P < 0.05$, ** $P < 0.01$, *** $P < 0.001$, n. s. No significant.

trigger the subsequent formation of glial scars, which has been proved principally constituted by the chondroitin sulfate proteoglycans (CSPGs) secreted by reactive glial cells, leading to chronic inhibition of axon regeneration following SCI [59,60]. Thus, we further analyzed the long-term immunoregulatory anti-glial scar effect of GHP@NSC hydrogel treatment by staining CS-56 to label CSPGs and GFAP to label astrocytes at 12 weeks post-injury. Immunofluorescence staining images (Fig. 6I) demonstrated that CSPG deposition beyond the GFAP region and into the lesion site was extremely limited in both the GHP and GHP@NSC groups, with the GHP@NSC group showing the most significant reduction. In contrast, the Blank group exhibited significant CSPGs deposition across the GFAP lesion boundary, densely extending into the lesion epicenter. It was concluded that the GHP hydrogel loaded with NSCs can modify the early-stage inflammatory storm and continuously respond to the inflammatory microenvironment following SCI, thereby reducing CSPGs enrichment in glial scar tissue at chronic stages and paving the way for axon sprouting.

2.7. Neurogenesis of the grafted NSCs in GHP

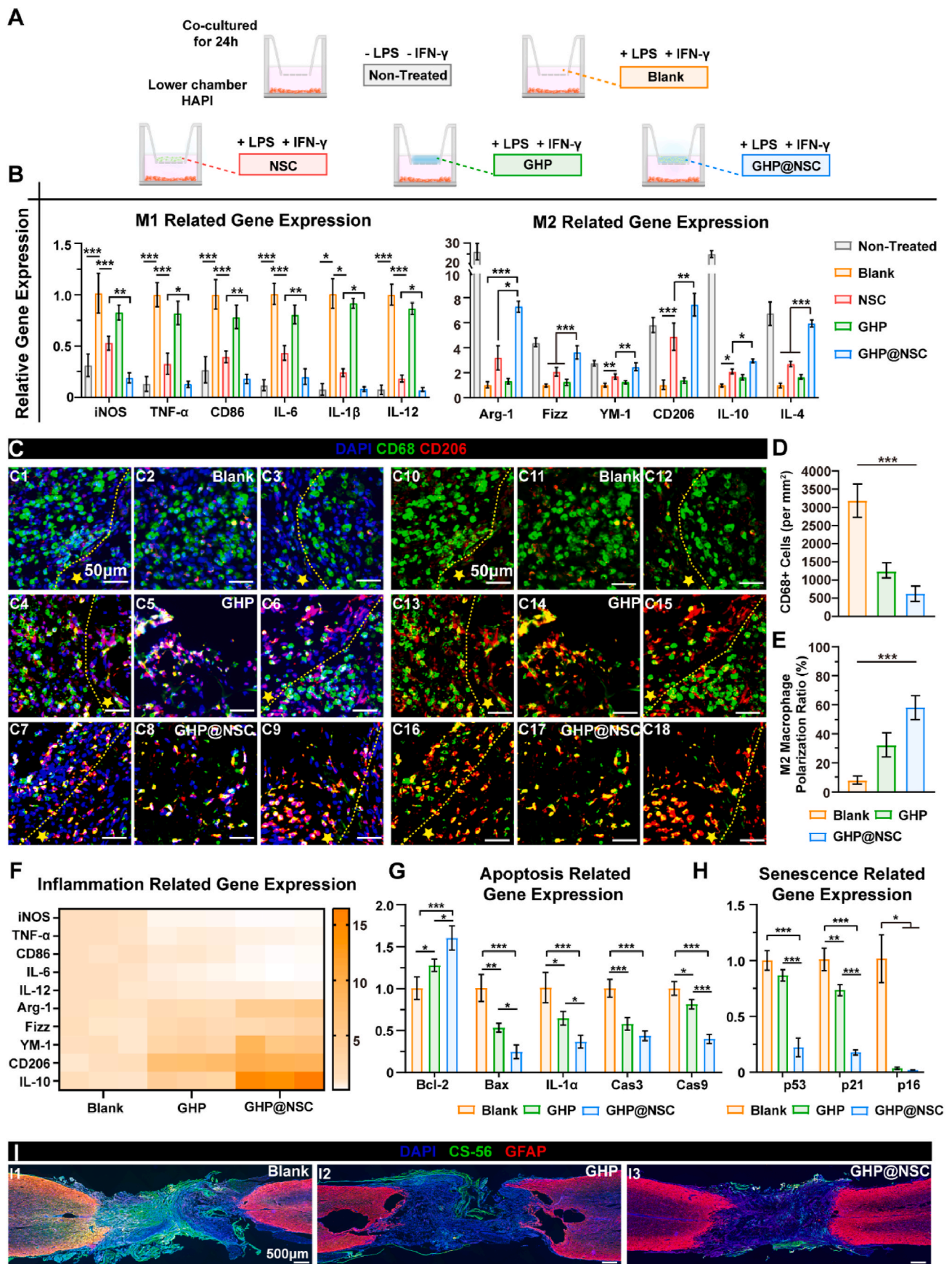
To investigate the capacity of GHP@NSC construct to encourage nerve regeneration and neuronal differentiation of NSCs during the intermediate stage of SCI, immunostaining of GFP, β -tubulin III (Tuj-1), and GFAP was performed to label grafted NSCs, nascent neurons, and astrocytes, respectively, at 4 weeks after SCI (Fig. 7A). Immunostaining results revealed that compared to the Blank group and GHP groups, the GHP@NSC group exhibited a significantly larger Tuj-1 positive-staining area and a smaller GFAP positive-staining area at the lesion site (Fig. 7A–C). Notably, a substantial number of GFP+ cells were observed and distributed evenly in the lesion epicenter of the GHP@NSC group (Fig. 7A and D), which indicated the dynamic nature of the GHP hydrogel and its protective effect on grafted NSCs. Moreover, the majority of NSCs exhibited a higher tendency to differentiate into neurons (>70 %) rather than astrocytes (Fig. 7D and E). The above results indicated that the 3D-printed GHP@NSC construct could provide synergistic dynamic biomechanics and biochemical cues for delivered NSCs, thereby permitting their adhesion, migration, and differentiation fate commitment during the intermediate stage of SCI.

Sufficient nutrition supply has been fully demonstrated to play a key role in promoting nerve repair [52]. On the one hand, synchronous vascularization is critical for the neural tissue regeneration process, as the supply of oxygen and nutrients to the lesion site facilitates the development of immature neurons [50]. Therefore, newly formed blood vessels labeled with rat endothelial cell antigen-1 (RECA-1) and newborn neurons labeled with Tuj-1 were used to evaluate the vascularization function of GHP@NSC constructs at 4 weeks post-injury (Fig. 7F). The RECA-1 positive-staining area in the GHP@NSC group was notably greater than other groups, and some newborn vasculature with lumen-like structures could be observed, synergistic with robust neural axons regeneration (Fig. 7F and J). Notably, the enhanced vascularization observed in the GHP group may be attributed to its structural dynamicity, which improves endothelial mechanotransduction and further promotes angiogenesis [61,62]. Additionally, the GHP@NSC construct stimulated the secretion of pro-angiogenic factors, such as VEGF and PDGF, facilitating the synergy between

angiogenesis and neurogenesis.

On the other hand, BDNF, NGF, NT-3, and other soluble neurotrophic factors secreted by the surrounding non-neuronal cells also play a critical role in constructing neurotrophic niches. P75 nerve growth factor receptor (p75^{NGFR}), a 75-kD transmembrane glycoprotein, is believed to interact with various soluble neurotrophic factors to greatly enhance the growth cone and neurite elongation [63,64]. Moreover, tropomyosin receptor kinase A (TrkA) and tropomyosin receptor kinase B (TrkB) are high-affinity receptors playing significant roles in neuronal development and synaptic plasticity by efficiently interacting with specific neurotrophic factors, like NGF activating TrkA and BDNF activating TrkB [65]. Therefore, we further evaluated the axonal sprouting and the expression of various neurotrophic factor receptors through co-staining growth-associated protein 43 (GAP43) with p75^{NGFR}, TrkA, and TrkB at 4 weeks post-injury (Fig. 7G–I) [66]. The immunofluorescence images showed that both the GHP and GHP@NSC groups presented a high density of double-positive signals for GAP43 and all three neurotrophin receptors in the lesion site, especially in the GHP@NSC group. However, in the Blank group, the GAP43+ regenerating axons, deprived of neurotrophin receptors, exhibited impaired growth cone spreading. The GHP@NSC group demonstrated comparably the highest expression levels of p75^{NGFR}, TrkA, and TrkB, revealing the significant refinement of the neurotrophic microenvironment in the lesion site (Fig. 7J). The qRT-PCR analysis also supported these results and provided further details (Fig. 7K and L). The results presented above might be mainly attributed to the synchronous vascularization induced by the GHP@NSC construct, which provided adequate nutrition and additional soluble nerve growth factors for the maturation of NSCs. In turn, the angiogenic bioactive factors such as VEGF secreted by NSCs enhanced the vascularization process, both contributing significantly to the reconstruction of the local neurovascular niche and the acceleration of nerve repair.

A crucial requirement for 3D-printed functional neural tissues is to ensure neuronal maturation and synapse formation between neurons while maintaining tissue structure. Thus, to investigate the long-term repair effects of the GHP@NSC construct on SCI, histological analysis was performed at 12 weeks after surgery. The mature nerve fibers and synapsin were investigated using neurofilament (NF) and synapse (SYN) staining, respectively. Additionally, in the GHP@NSC group, GFP was applied to distinguish between grafted cells and host cells (Fig. 7M). In the Blank group, the repaired tissue showed poor organization and lacked typical NF-positive signals. Conversely, in the GHP group, more NF-positive signals in the lesion area were observed, suggesting the improvement of nerve regeneration; however, the NF/SYN co-positive signals were limited, and the cavities still existed in the repaired tissue. Remarkably, in the GHP@NSC group, abundant NF-positive neurofilaments from the lesion boundary were in directional arrangement and migrated into the lesion core, densely contacting NF/GFP double-positive signals in the injured area, making the boundary between adjacent host tissue and regenerated tissue indistinguishable (Fig. 7N and O). Moreover, statistical analysis showed that the GHP@NSC group had the highest proportion of NF/SYN double-positive cells, approximately 16 %, in sharp contrast to the Blank and GHP groups (Fig. 7M and O). These results suggested that the GHP@NSC construct therapeutic strategy could induce NSCs to differentiate into mature neurons and promote synaptic formation with regenerated host neurons, achieving



(caption on next page)

Fig. 6. Regulation of local inflammatory responses and modulation of inflammation-triggered secondary injury. A) Schematic diagram and grouping of transwell immunoregulation assessment by HAPI cells indirectly co-cultured with different treatment groups *in vitro*. B) Relative pro-inflammatory (M1) and anti-inflammatory (M2) gene expression of HAPI cells in different co-culture groups at 24 h cultivation *in vitro*. C) Representative CD68 (green), CD206 (red), and DAPI (blue) immunofluorescence staining images of the rostral, lesion, and caudal sites of Blank, GHP, and GHP@NSC groups at 1-week post-surgery *in vivo*; the yellow pentagrams indicate the lesion site and the dotted lines mark the boundaries between the lesion site and the host spinal cord. D, E) Quantitative analysis of the CD68-positive cells density (D) and the polarization ratio of M2 phenotype macrophage (E) from the enlarged view. F–H) Relative expression of inflammation (F), apoptosis (G), and senescence (H) related genes in tissue samples of different groups at 1 week post-surgery. I) Representative CS-56 (green), GFAP (red), and DAPI (blue) immunofluorescence staining images of the longitudinal section at 12 weeks post-surgery. Quantification data represent mean \pm SD. *P < 0.05, **P < 0.01, ***P < 0.001, n. s. No significant.

extensive and robust nerve repair and neural relays construction throughout the lesion epicenter. This can be attributed to the intrinsic biomechanical and biochemical properties of the GHP@NSC construct. Specifically, its self-healing and macroscopic stability properties ensure that the GHP@NSC construct maintains tissue structure in the inhospitable lesion area for a long-term period, providing important topographical guidance and mechanical support for neurodevelopment. Additionally, the living constructs significantly promoted neurogenesis and prevented the formation of histological cavities in the lesion sites, revealing the ideal and unique balance between the rate of degradation and matrix remodeling. Furthermore, the orchestrated ECM-like dynamic molecular structure and biochemical cues of the GHP@NSC living construct also enhance the mechanically induced processes of cell-matrix and cell-cell interactions for the transplanted NSCs, thereby permitting their long-term cell fate commitment, functional synapse formation, and graft-host integration.

2.8. Reconstruction of functional neural network with GHP@NSC treatment

The complex neural networks in the spinal cord regulate a variety of physiological functions [67,68]. Therefore, understanding functional maturation and connectivity in 3D-printed neural tissues is vital for the application of NSC-derived constructs in regenerative medicine. In the central nervous system, the myelin sheath is essential for the maintenance of normal axonal function and the saltatory conduction of neuronal signals [69]. The remyelination of regenerated nerve fibers after SCI plays a critical role in neuron functional maturation and neural network reconstruction [5]. Transversely sections of regenerated tissues from the lesion site, at 12 weeks post-surgery, were evaluated using toluidine blue staining (Fig. 8A) and transmission electron microscopy (Fig. 8B), respectively. Abundant regenerated nerve fibers were wrapped in smooth myelin sheath in the GHP@NSC group. However, in the GHP group, myelin sheath structures were thin, small, and presented a wavy appearance. In the Blank group, such structures were nearly absent, with debris of mixed composition instead. Quantitative analysis revealed that the GHP@NSC group exhibited the highest nerve fiber regeneration capacity and remyelination ratio compared to other groups (Fig. 8C and D). The area-based G-ratio (nerve fiber/the whole myelinated nerve fiber area) analysis further indicated the highest degree of myelin sheath maturation in the GHP@NSC group (Fig. 8E and F). Subsequently, we examined these structures in the GHP@NSC group using longitudinal sections of the lesion epicenter by applying immunostaining for GFP (indicating grafted NSCs), NF (indicating nerve fiber), and myelin basic protein (MBP, indicating myelin sheath) (Fig. 8G). The strong colocalization signals of GFP, NF, and MBP verified the generation of mature, functional neurons via differentiation of grafted NSCs, paving the way for the formation of neural network structures.

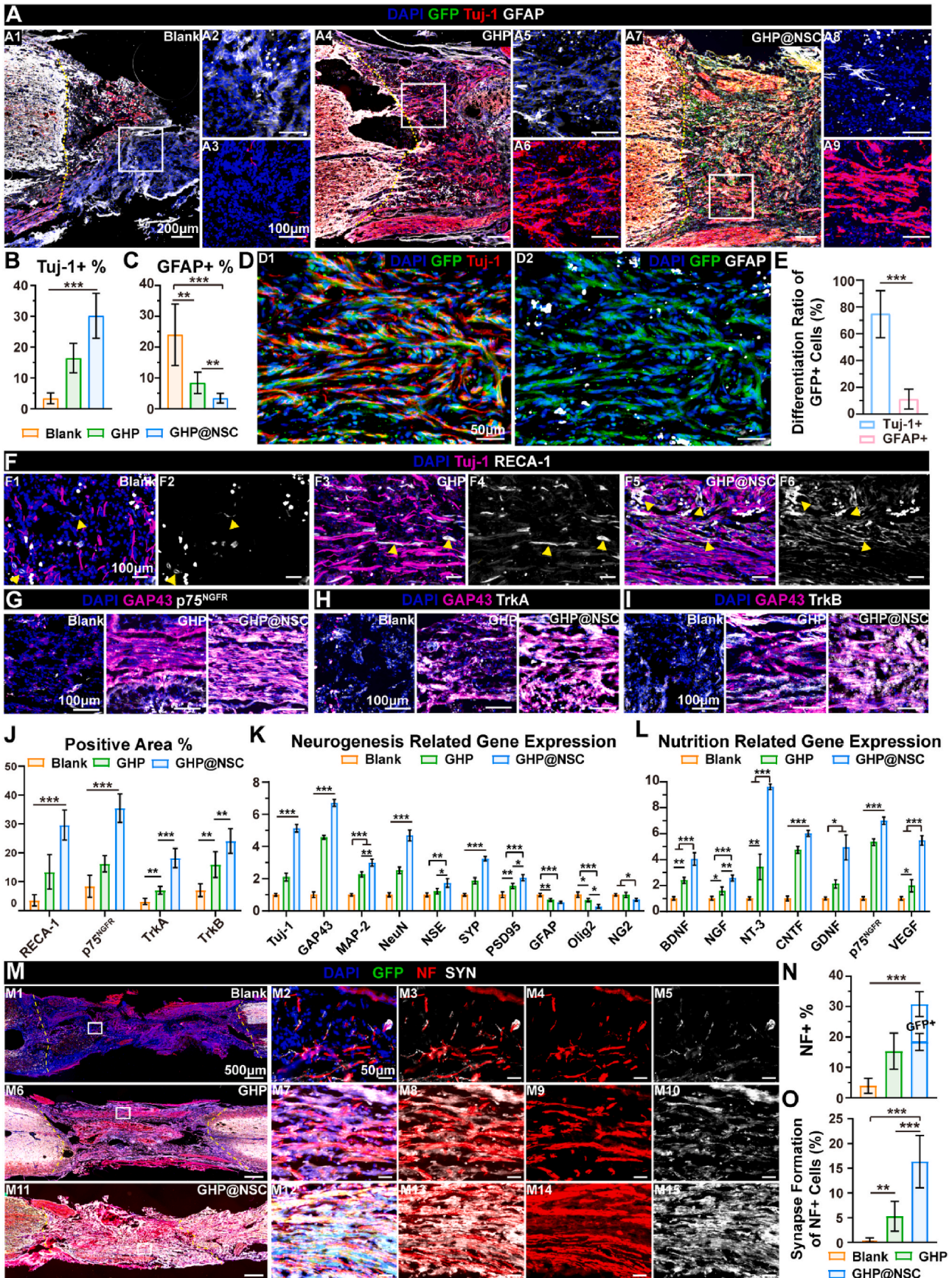
It is well established that motor and sensory functions of the spinal cord are mediated by the interactions between different populations of neuronal types. Building on the demonstrated therapeutic efficacy of the GHP@NSC construct, we aimed to further assess whether these regenerated nerve fibers in the GHP@NSC group are the primary functional neuronal types that form spinal neural networks. It was found that the GHP@NSC construct facilitated sensory and motor neuron regeneration

at the lesion site, as evidenced by the immunostaining of 5-hydroxytryptamine (5-HT), tyrosine hydroxylase (TH), calcitonin gene-related peptide (CGRP), and choline acetyltransferase (ChAT) (Fig. 8H–K). Notably, these different types of functional neurons mostly co-expressed GFP (Fig. 8H4, 8I4, 8J4, and 8K4), indicating that these functional neurons were mostly derived from the 3D bioprinted GHP@NSC construct, which not only revealed the ultimate fate commitment of exogenous NSCs modulated with GHP hydrogel *in vivo*, but also indicated the necessity of living construct transplantation. Moreover, some of these functional nerve fibers exhibited the capability of synapse formation (Fig. 8H5, 8I5, 8J5, and 8K5), which might potentially contribute to neural network construction. Furthermore, qRT-PCR analysis showed that the mRNA expression of functional neuron-related markers (MBP, myelin oligodendrocyte glycoprotein (MOG), 5-HT, TH, CGRP, ChAT, and gamma-aminobutyric acid (GABA)) was significantly up-regulated in the GHP@NSC group (Fig. 8L), providing evidence for the long-term maintenance potential of neuronal subtypes in the GHP@NSC constructs.

In addition to the functional maturation of regenerated neurons, the axonal connectivity also plays a critical role in the reconstruction of primitive sensory-motor neural circuits after SCI [70]. To determine the neural circuit connectivity following treatment with the GHP@NSC construct, we traced the descending propriospinal axons using biotinylated dextran amine (BDA) anterograde tracing, and the ascending propriospinal axons using cholera toxin B subunit (CTB) retrograde labeling. The BDA-positive and CTB-positive axons were clearly visible in the rostral, lesion epicenter, and caudal regions of the host spinal cord (Fig. 8M and N). These observations indicated improved connectivity of descending and ascending compensatory neural circuits following GHP@NSC construct treatment, leading to effective recovery of motor and sensory functions of SCI rats. Moreover, the diffusion tensor tractography (DTT) of MRI results in the GHP@NSC group suggested that blue-colored anterior-posterior aligned diffusion tensor imaging (DTI) signals extended directionally across the lesion site from rostral to caudal stumps of the spinal cord, in sharp contrast to the other groups (Fig. 8O). Collectively, these findings suggested that GHP@NSC construct implantation fostered the integration of regenerated descending and ascending interneurons into motor-sensory neural circuits, further boosting the formation of functional neural networks and ameliorating connectivity in the damaged spinal cord.

3. Conclusion

In summary, we successfully developed a 3D bioprinted dynamic living construct that exerted dynamic biomechanical and instructive biochemical cues to modulate the encapsulated NSCs self-organized toward a functional neural network for spinal cord injury repair. By integrating reversible dynamic Schiff-base bonds, stable covalent bonds, and bioactive motifs, we fabricated an ECM-mimicking bioink with microscopic dynamicity, enhanced cell-adaptability, excellent bioprintability, and cell-instructive properties. The dynamic characteristics of the bioink create an adaptable network that enables the encapsulated NSCs to sense biomechanical signals from the 3D matrix more effectively, thereby enhancing active cell-matrix interactions. The instructive biochemical cues, N-cadherin-mimicking and BDNF-mimicking peptides, specialized for capturing the native NSCs niche, significantly



(caption on next page)

Fig. 7. Fate of grafted NSCs, establishment of suitable niche, and enhancement of nerve regeneration *in vivo*. A) Representative GFP (green), Tuj-1 (red), GFAP (white) and DAPI (blue) immunofluorescence staining images of Blank, GHP, and GHP@NSC groups at 4 weeks post-surgery, A2, A3, A5, A6, A7, and A8 are enlarged images of A1, A4, and A7; the dotted lines mark the boundaries between the lesion site and the host spinal cord. B, C) Quantitative analysis of Tuj-1-positive (B) and GFAP-positive (C) area percentage from the enlarged view. D) Representative GFP (green), Tuj-1 (red), DAPI (blue) (D1) and GFP (green), GFAP (white), DAPI (blue) (D2) immunofluorescence staining images of the lesion site in GHP@NSC group rat at 4 weeks post-surgery. E) Quantitative analysis of grafted NSC differentiation ratio measured by the percentage of GFP-Tuj-1 or GFP-GFAP co-stained cell numbers over the total GFP-labeled NSC numbers. F) Representative Tuj-1 (purple), RECA-1 (white), and DAPI (blue) immunofluorescence staining images of the lesion sites at 4 weeks post-surgery; the yellow triangles refer to revascularized blood vessel tissues. G–I) Representative DAPI (blue) and GAP43 (purple) immunofluorescence staining images of the lesion site of Blank, GHP, and GHP@NSC groups co-staining with p75^{NGFR} (white) (G), TrkA (white) (H), and TrkB (white) (I) at 4 weeks post-surgery. J) Quantitative analysis of RECA-1, p75^{NGFR}, TrkA, and TrkB positive area percentage from the corresponding immunofluorescence staining images. K, L) Relative expression of neurogenesis (K) and nutrition (L) related genes in tissue samples of different groups at 4 weeks post-surgery. M) Representative GFP (green), NF (red), SYN (white), and DAPI (blue) immunofluorescence staining images of the longitudinal section at 12 weeks post-surgery, M2–M5, M7–M10, and M12–M15 are enlarged views of M1, M6, and M11; the dotted lines mark the boundaries between the lesion site and the host spinal cord. N) Quantitative analysis of NF-positive area and GFP-NF co-stained area percentage from the enlarged view. O) Quantitative analysis of the synapse formation ratio within the NF-positive cells from the enlarged views. Quantification data represent mean \pm SD. * $P < 0.05$, ** $P < 0.01$, *** $P < 0.001$, n. s. No significant.

strengthened NSCs' mechanotransduction, cell-cell adhesion, and neurotrophic secretion, thus facilitating the self-organization of a functional neural network within the 3D bioprinted constructs. Additionally, our *in vivo* results demonstrated that the 3D bioprinted construct refined the immune microenvironment, remodeled the neurotrophic niche, and reconstructed functional neural circuits, effectively promoting motor and sensory function recovery. In aggregate, our findings underscore the significance of adaptable dynamic biomechanics and instructive biochemical cues in designing functionalized bioinks, which directly impact the effectiveness of 3D bioprinted constructs in tissue regeneration.

4. Materials and methods

4.1. Synthesis of GelMA and OHA

GelMA was synthesized as previously described [71]. In brief, 10 g type A porcine skin gelatin (Sigma-Aldrich, USA) was dissolved in 100 mL Dulbecco's phosphate-buffered saline (DPBS, Invitrogen, USA) at 50 °C, and 8 mL of methacrylic anhydride (MA, Sigma-Aldrich, USA) was added to the gelatin solution dropwise while stirring. The reaction was held for 3 h at 50 °C, and terminated with 5x DPBS addition for dilution. After dialyzing with a 12–14 kDa cut-off dialysis membrane against deionized water at 50 °C for 7 days, the solution was lyophilized for 1 week to obtain the GelMA sponge.

To obtain oxidized HA (OHA), 1 g of hyaluronic acid (HA, 100–200 kDa, MACKLIN, China) was dissolved in 90 mL water at room temperature [72]. Then 0.535 g of NaIO₄ (Sigma-Aldrich, USA) dissolved in 10 mL water was added dropwise to the HA solution while stirring. The reaction proceeded for 24 h at room temperature in the dark, followed by adding 2 mL of ethylene glycol to quench the unreactive NaIO₄. The solution was then dialyzed with a 7 kDa cut-off dialysis membrane against deionized water for 3 days and lyophilized for 3 days for further use.

Proton nuclear magnetic resonance (¹H NMR) was performed to verify the successful synthesis of GelMA and OHA. At room temperature, the ¹H NMR spectra were recorded with a 600 M NMR spectrometer (JNM-ECA600, JEOL Ltd., Japan).

4.2. Synthesis of peptide

A brain-derived neurotrophic factor-mimicking peptide (RGI, H₂N-GGGGRGIDKRHWNSQ), and an N-cadherin-mimicking peptide (HAVDI, H₂N-GGGGHAVDI) were custom-synthesized and purified by Scilight-Peptide Co., Ltd (Beijing, China). The purity of the peptides was confirmed by analytical high-performance liquid chromatography (HPLC) to qualify the standard of purity >95 %.

4.3. Preparation and characterization of G, GH, and GHP prepolymer

The prepolymer solutions for three groups of hydrogels were prepared and named correspondingly: G (5 % GelMA), GH (5 % GelMA and 1 % OHA), or GHP (5 % GelMA, 1 % OHA, 3 mM RGI, and 3 mM HAVDI). The weight/volume percentage concentration (w/v%) was applied to calculate the hydrogel formula, and phosphate-buffered saline (PBS, Invitrogen, USA) was used as the solvent. To determine the conjugation between GelMA, OHA, and peptides, ¹H NMR and Fourier Transform Infrared Spectroscopy (FTIR) assessment was performed. The ¹H NMR evaluation was carried out with GelMA, OHA, RGI peptide, HAVDI peptide, GH prepolymer, and GHP prepolymer solution in D₂O. GH prepolymer and GHP prepolymer were further lyophilized for FTIR evaluation. Peptide powders (RGI and HAVDI) and lyophilized GelMA, OHA, GH prepolymer, and GHP prepolymer were mixed with 100X (w/v) KBr, respectively. FTIR spectra were obtained using the FTIR spectrometer (TG-MS-FTIR-70, NETZSCH Groups, Germany), with wave-numbers ranging from 4000 to 400 cm⁻¹ at 1 cm⁻¹ resolution and 32 scans per spectrum.

The secondary structure of peptides was investigated through circular dichroism analysis. The sample of GH prepolymer, GHP prepolymer, and the mixed solution of RGI & HAVDI peptides were prepared in the concentration of 0.01 % (w/v). Then, 200 μ L of corresponding samples were added into the quartz cuvette with a path length of 1 mm. CD measurement was carried out by Chirascan Plus (Applied Photophysics, Leatherhead, UK) at room temperature, and the scans ranged from 180 to 260 nm. The negative staining method was applied to obtain the peptide nanofiber structures with the transmission electron microscope (TEM, TECNAI Spirit, FEI, Czech Republic). The 0.01 % (w/v) GHP prepolymer and RGI & HAVDI peptide solution were prepared as described above. Next, 10 μ L of the sample was dropped on the copper mesh, and the surplus liquid was siphoned off using filter paper after 2 min. Subsequently, redyeing of the sample was performed with the addition of 10 μ L 2 % (v/v) uranyl acetate to the copper mesh for 30 s. After removing the droplet, samples were dried completely overnight for further observation under TEM.

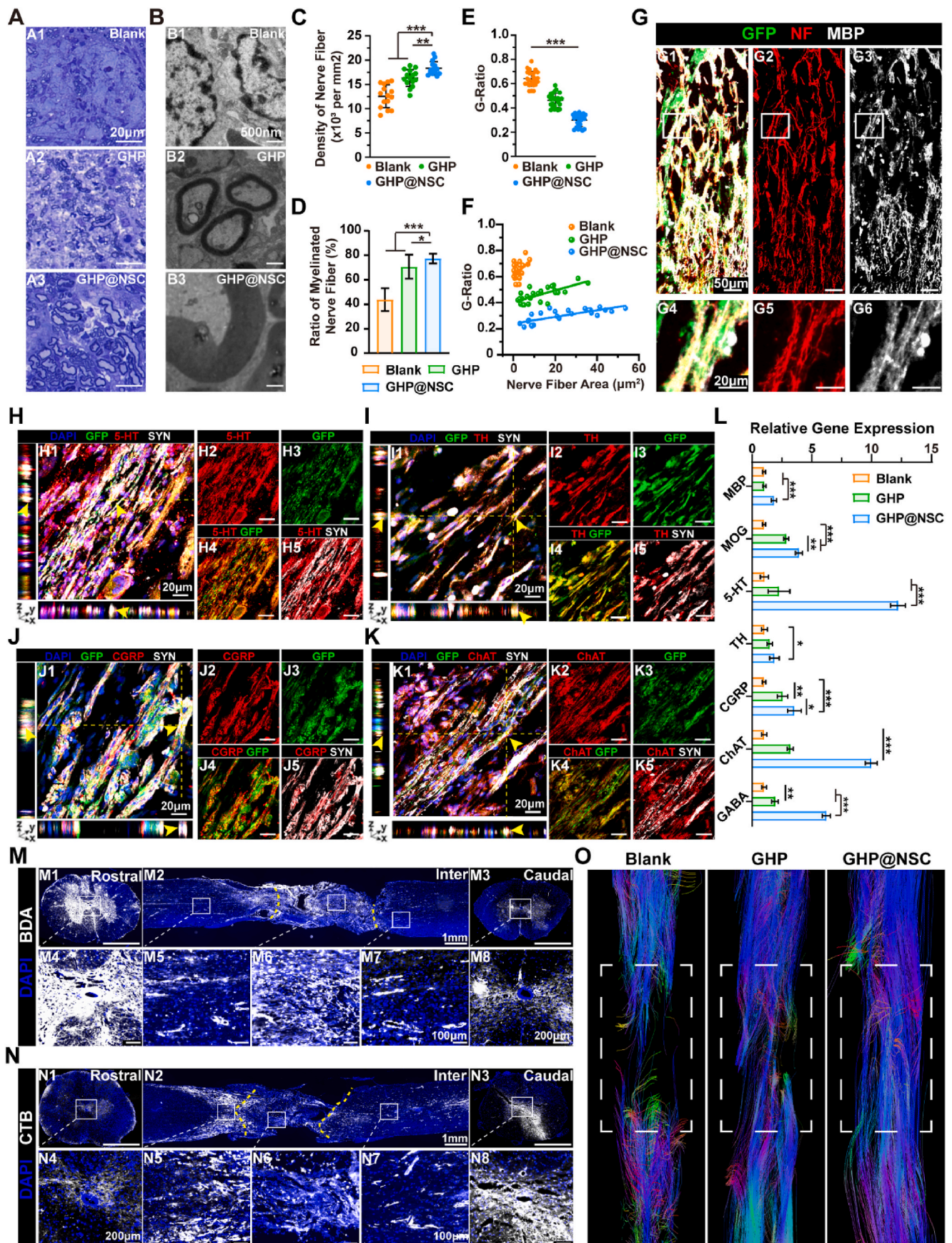
4.4. Formation and characterization of G, GH, and GHP hydrogel

4.4.1. Hydrogel formation

The 0.1 % (w/v) Lithium phenyl-2,4,6-trimethylbenzoylphosphinate (LAP, photoinitiator, MERYER, China) was added to the prepolymer solution of G, GH, and GHP prepared as described above. G, GH, and GHP hydrogels were formed with the 10 mW/cm² UV irradiation for 50 s by EFL-LS1602 (EFL, China).

4.4.2. Peptide binding and releasing

The binding rate of RGI and HAVDI peptide immobilized onto the GHP hydrogel was evaluated via mass spectrum in ACQUITY UPLC I-Class PLUS (StepWave, China). GHP hydrogel samples (n = 5) were



(caption on next page)

Fig. 8. Myelin regeneration and functional neural network reconstruction. A, B) Toluidine blue-stained (A) and TEM images (B) of transverse sections at the lesion site of the Blank, GHP, and GHP@NSC groups. C, D) Quantitative analysis of nerve fiber density (C) and the myelination ratio (D) from Toluidine blue-staining images. E, F) Quantitative analysis of the area-based G-ratio (E) and the scatter diagram of G-ratio as a function of nerve fiber area (F) from TEM images. G) Representative GFP (green), NF (red), and MBP (white) immunofluorescence staining images of the lesion site of GHP@NSC group at 12 weeks post-surgery. G4-G6 are the enlarged images of G1-G3. H-K) Representative DAPI (blue), GFP (green), and SYN (white) immunofluorescence staining Z-stack images of the lesion site of GHP@NSC group co-staining with 5-HT (red) (H), TH (red) (I), CGRP (red) (J), and ChAT (red) (K) at 12 weeks post-surgery. L) Relative expression of myelination and functional neuron-related genes in tissue samples of different groups at 12 weeks post-surgery. M, N) Representative overview of the longitudinal and transverse section of the rostral, lesion, and caudal sites in the GHP@NSC group immunostained with BDA (M) and CTB (N) at 12 weeks post-surgery; M1, M3, N1, and N3 are transverse sections, M2 and N2 are longitudinal sections, M4, M5-M7, M8, N4, N5-N7, N8 are enlarged images of M1, M2, M3, N1, N2, and N3 respectively; the dotted lines mark the boundaries between the lesion site and the host spinal cord. O) DTI trace images of spinal cord tissue vertical sections in different groups at 12 weeks post-surgery; the white rectangles indicate the lesion sites. Quantification data represent mean \pm SD. * $P < 0.05$, ** $P < 0.01$, *** $P < 0.001$, n. s. No significant.

prepared and soaked in PBS (pH = 7.4) for 2 h immediately after gelation. Subsequently, the supernatant was collected and the mass spectrum assessment was carried out to determine the concentration of uncombined peptide. For the peptide-releasing profile, GHP hydrogel samples ($n = 5$) were immersed in 2 mL PBS (pH = 7.4). Then, 200 μ L of supernatant was collected respectively at different preset time intervals (1, 2, 3, 7, 14, and 28 days) and the same amount of fresh PBS was added to the corresponding system. The collected supernatant was used for HPLC (Agilent 1260, USA) assessment to measure the concentration of RGI and HAVDI peptide.

4.4.3. Hydrogel morphology

Hydrogel of G, GH, and GHP was dried with a samdri-PVT-3D CO₂ critical point dryer (Tousimis, USA) after dehydrating in successive concentrations of ethanol (75 %, 80 %, 85 %, 90 %, 95 %, and 100 %). The fresh cross-sectional surface was further revealed for further morphology observation. Then, 10 nm platinum film-coating was sputtered on the surface, and the surface morphology of hydrogels was observed using field emission scanning electron microscopy (SEM, CarlZeiss, Oberkochen, Germany). The internal morphology of the hydrogel was monitored using a transmission electron microscope (TEM, TECNAI Spirit, FEI, Czech Republic). Hydrogels were successively fixed with 2.5 % glutaraldehyde for 3 h and 1 % osmium tetroxide solution for 1 h. After dehydration, samples were embedded with Epon 812 epoxy resin (Fluka, Münster, Germany), and cut into 70 nm-thick transverse slices. Finally, the slices were stained with uranyl acetate and prepared for TEM observation.

4.4.4. Water content and swelling ratio test

The water content of G, GH, and GHP hydrogels ($n = 3$ in each group) was characterized by measuring the wet weight after full hydration and the dry weight after lyophilization, then calculated with the following equation:

$$\text{Water content (\%)} = (\text{wet weight} - \text{dry weight}) / \text{initial wet weight}$$

The initial weight of the hydrogel right after gelation and the final weight of the hydrogel soaked in water for 36 h were noted. Subsequently, the swelling ratio of G, GH, and GHP hydrogels was calculated with the following equation:

$$\text{Swelling Ratio (\%)} = (\text{Initial weight} - \text{final weight}) / \text{initial weight}$$

4.4.5. Contact angle assessment

The water contact angles of G, GH, and GHP hydrogel ($n = 3$ in each group) were measured using an OCA15Pro Optical contact angle tester (Dataphysics, German). A water drop was made on the hydrogel sample at ambient atmosphere and temperature. Images of water drops were recorded, followed by calculation and analysis of contact angles ($n = 3$ in each group).

4.4.6. Degradation assessment

G, GH, and GHP hydrogels ($n = 3$ in each group) were immersed and

incubated in the condition of PBS with 0.1 mg/mL collagenase (BioFroxx, Guangzhou, China) and 0.1 mg/mL hyaluronidase (BioFroxx, Guangzhou, China) at 37 °C. The concentration of enzymes and the degradation condition were selected based on the previous literature [73,74]. The wet weight of the hydrogel was monitored respectively over time.

4.4.7. Rheology assessment

All rheology assessment in this study was performed with a rheometer (MCR302e, Anton Paar GmbH, Graz, Austria) ($n = 3$ in each group). Rheological properties of the hydrogels were examined with an 8 mm-diameter parallel plate at 37 °C. Storage (G') and loss (G'') moduli were recorded in a dynamic amplitude sweep (0.01%–1000 % strain at 1 Hz) and frequency sweep test (0.1–10 Hz at 1 % strain), followed by the statistical analysis of storage modulus of the corresponding hydrogel at 1 % strain and 1 Hz. To investigate the microscopical self-healing capability of hydrogels, a three-cycle step-strain time sweep was performed at 1 Hz with a low strain of 1 % and a high strain of 500 %. For the stress relaxation assessment, a time sweep test was conducted at a constant strain of 10 %. The relaxation time of the hydrogels is defined as the time taken for the stress to decrease to 50 % of its initial value. To test the gelation conditions of the G, GH, and GHP prepolymers, the storage and loss moduli were measured using a temperature sweep (1 Hz, 0.1 % strain) with a heating rate of 5 °C/min, ranging from 10 °C to 40 °C. The UV sensitivity of these prepolymers was evaluated using oscillatory time sweeps (1 Hz, 0.1 % strain), with UV irradiation (10 mW/cm²) applied between 100 and 150 s. The viscosity of the prepolymers was recorded using an amplitude sweep at 28 °C, with a shear rate ranging from 0.1 to 100 s⁻¹.

4.4.8. Compression assessment

G, GH, and GHP hydrogels ($n = 3$ in each group) were prepared in cylindrical shapes with a diameter of 10 mm and a height of 5 mm. The compressive test was performed using a dynamic mechanical analysis (DMA, Q800 V²¹.2 Build 88, TA Instruments, USA) in the Stress/Strain module. The compressive analysis was conducted at a constant strain rate of -20 %/min. The stress-strain curve was plotted, and the Young's Moduli were determined by calculating the slope of the linear elastic region of the stress-strain curve.

4.4.9. Self-healing assessment

Two identical hydrogel samples of G, GH, and GHP were prepared respectively with distinguishable colors for macroscopical self-healing assessment. Then, samples were cut into halves. Two half-pieces were put together for 2 h, and the cross-section was observed for integration.

4.4.10. FITC-BSA loading and releasing assessment

Fluorescein isothiocyanate isomer-bovine albumin (FITC-BSA, M.W. 67 k, MeilunBio, China) was used to evaluate the substance exchange capability of G, GH, and GHP hydrogel. For loading assessment, FITC-BSA was diluted in PBS to 5 mg/mL. The G, GH, and GHP hydrogel samples ($n = 3$ in each group) were prepared in a transparent glass bottle, and immersed in 5 mL FITC-BSA solution at 37 °C. Then, 10 μ L of the supernatant was collected at every preset time interval (10 min, 1 h,

2 h, 4 h, 8 h, and 12 h). The fluorescence intensity of the supernatant was measured with the microplate reader (Infinite F50, Tecan, Switzerland) to determine the remaining un-loaded FITC-BSA concentration. For releasing assessment, FITC-BSA loaded hydrogel samples ($n = 3$ in each group) were prepared by dissolving 5 mg/mL FITC-BSA into the G, GH, and GHP precursor solution before gelation in a transparent glass bottle. Subsequently, samples were immersed in PBS at 37 °C and the fluorescence intensity of 10 μ L supernatant was detected every preset time intervals (10 min, 1 h, 2 h, 3 h, 4 h, 6 h, 8 h, 12 h, 24 h, and 36 h) to determine the released concentration of FITC-BSA.

4.5. Isolation and culture of neural stem cells

Neural stem cells (NSCs) were isolated as previously described [30]. In brief, the fetal (embryonic Day 14) SD rats were separated, endocranium and blood vessels were stripped, and the hippocampus was extracted gently on ice. Extracted hippocampal tissues were placed in ice-cold PBS, cut into small pieces, and digested with 0.05 % EDTA-/Trypsin (Gibco, USA) for 10 min at 37 °C. After centrifugating at $200 \times g$ for 5 min, the cells were cultured in proliferative NSC medium (DMEM/F12 medium (Gibco, USA) containing 2 % B27 (Gibco, USA), 1 % N2 (Gibco, USA), 1 % penicillin-streptomycin (PS, Sigma-Aldrich, St. Louis, MO), 20 ng/mL basic fibroblast growth factor (bFGF, Solarbio, China), and 20 ng/mL epidermal growth factor (EGF, Solarbio, China)). NSCs were cultured in an incubator with 5 % CO₂ at 37 °C, and half of the medium was changed every 2 days. After 7–10 days of propagation, NSC spheres were digested with accutase (Invitrogen, USA) into single cells and passaged with fresh proliferation NSC medium. Subsequently, NSC spheres formed after 7 days of culture were collected randomly and stained with Nestin (1:100, sc-23927, Santa Cruz, USA) to identify NSCs. Images were observed and captured with confocal laser scanning microscopy (LSM980 Airyscan2, Zeiss, Germany).

For the *in vitro* study, NSCs were cultured in a proliferation NSC medium and centrifugated into single cells before usage. For *in vivo* transplantation, we selected a well-established GFP-labeling method to trace exogenous NSC, which is confirmed for its stability, sustainability, and non-interference with cellular function [75]. To be detailed, the NSCs were cultured adherently in a proliferative medium containing lentiviral particles (pLVGFP/Puro-CMV, Cyagen Biosciences, China) and 5 μ g/mL of polybrene for 16 h at a multiplicity of infection (MOI) of 50.

4.6. 3D bioprinting procedure

A commercial 3D printing system (Bioscaffold, GeSim, Germany) was employed to print 3D bio-constructs in this study. For *in vitro* experiments, G@NSC, GH@NSC, and GHP@NSC were fabricated in a biosafety cabinet after sterilization with UV and 75 % ethanol. The prepolymer solutions of G, GH, and GHP were prepared as mentioned above in the preparation section, with 0.1 % (w/v) LAP addition, and stored at 37 °C for further NSC encapsulation. Then, the prepolymer solutions were used to resuspend NSCs (2×10^7 cells/mL) to form a homogeneous bioink. The plastic cylinder was equipped with a 260- μ m nozzle, and loaded with NSC-laden bioink. Bioprinting operation was carried out with the temperature maintained at 28 °C around the plastic cylinder and at 10 °C in a 12-well culture plate on the print platform, respectively, for bio-construct printing and collection. 3D bio-construct was subsequently cultivated with a culture medium in the incubator for further experiments. The parameters for 3D bio-construct printing for *in vitro* experiments were as follows: extrusion pressure: 5 kPa; printing speed: 20 mm/s; strand height: 0.15 μ m; curing time: 10 s per layer; UV intensity: 10 mW/cm². A grid structure model with a side length of 10 mm, height of 1 mm, and stand distance of 1 mm was devised, and the adjacent strands were arranged vertically. For *in vivo* transplantation, the bio-constructs were fabricated as stated above with the same parameters for 3D printing. The model was designed to resemble the spinal

cord, with a cuboid (length = 4 mm, width = 2 mm, height = 2 mm) constructed layer-by-layer with parallel strands (strand distance = 400 μ m).

4.7. Live/dead staining *in vitro*

The viability of the encapsulated NSCs in a 3D construct was evaluated with Live/Dead™ staining. Briefly, after immediate 3D printing and cultivation of 1, 3, and 7 days, the G@NSC, GH@NSC, and GHP@NSC constructs ($n = 3$ in each group) were incubated with Calcein AM (2 μ m) for 20 min, respectively. After rinsing with PBS three times, incubation with propidium iodine (PI) (2 μ m) was carried out for 10 min, and washed with PBS three times once more. Scanning confocal laser microscopy (Zeiss, Airyscan2-LSM980, Germany) was used to photograph the images for further analysis. Imaris 9.3.1 (Oxford Instruments, UK) was applied for the cell-counting of live cells and total cells, and the cell viability was calculated by dividing the number of live cells by the total number of cells at each corresponding time point.

4.8. Quantitative reverse transcription polymerase chain reaction (qRT-PCR) *in vitro*

To investigate the mechanotransduction and differentiation behavior of NSCs encapsulated in 3D bio-construct, G@NSC, GH@NSC, and GHP@NSC were cultured in the corresponding medium. After 3, 7, and 14 days of cultivation, G@NSC, GH@NSC, and GHP@NSC bio-construct ($n = 3$ in each group) were collected and the total RNA of encapsulated NSCs was extracted with the RNA simple Total RNA Kit (Tiangen, China) respectively, followed by reverse cDNA transcription with FastKing RT kit (Tiangen, China). The qRT-PCR was carried out by a CFX96 real-time PCR detection system (Bio-Rad, USA) with the appliance of SYBR Green supermix (Bio-Rad, USA). Relative gene expression for target genes was normalized by the housekeeping gene (GAPDH), and the analysis was performed using the 2^{- $\Delta\Delta$ Ct} method. The primer sequences are presented in Table S1, Supporting Information.

4.9. Immunofluorescence staining *in vitro*

For immunofluorescence staining, G@NSC, GH@NSC, and GHP@NSC constructs were cultured in a differentiation medium for 3 and 7 days respectively. Subsequently, the constructs were sequentially performed with fixation in 4 % paraformaldehyde (PFA) for 1 h at 4 °C, permeabilization in 0.3 % Triton X-100 (Sigma, Germany) for 10 min, and blockage in 10 % normal goat serum (Solarbio, China) for 1 h. Then samples were incubated in primary antibodies overnight at 4 °C, washed in PBS three times, and immunostained with corresponding secondary antibodies and DAPI (sc-74421, Santa Cruz, USA) for 1 h in the dark at room temperature. Scanning confocal laser microscopy (LSM980 Airyscan2, Zeiss, Germany) was applied for image taking, and Imaris 9.3.1 (Oxford Instruments, UK) was used for image quantification analysis. The primary and secondary antibodies are presented in Table S2, Supporting Information.

4.10. Bioprinted construct morphology

For the observation of NSC morphology encapsulated in 3D bio-constructs, G@NSC, GH@NSC, and GHP@NSC were cultured in the differentiation DMEM/F12 medium with 10 % fetal bovine serum (FBS) and 1 % PS for 7 and 14 days. Then, bio-constructs were fixed with 4 % PFA for 1 h, permeabilized with 0.3 % Triton X-100 for 15 min, and blocked with 10 % normal goat serum for 1 h successively. Samples were incubated in Rhodamine Phalloidin (RP, Solarbio, China) and DAPI in the dark for 40 min. Finally, the NSC morphology within the 3D bio-constructs was observed and captured with scanning confocal laser microscopy (LSM980 Airyscan2, Zeiss, Germany). Further, the morphology of NSCs encapsulated in a 3D bio-construct was examined

by SEM. G@NSC, GH@NSC, and GHP@NSC cultured in a differentiation medium were fixed with 2.5 % glutaraldehyde for 2 h after 7 days of cultivation. Samples were then dehydrated and dried as described above, followed by the observation with SEM.

4.11. Enzyme-linked immunosorbent assay *in vitro*

The BDNF, NGF, NT-3, and CNTF secretion of the encapsulated NSCs in different 3D bio-constructs (G, GH, and GHP; $n = 3$ for each group) were measured respectively with enzyme-linked immunosorbent assay (ELISA) kits (Meimian, China). The supernatant of the medium culturing NSC-laden 3D bio-construct was collected on Day 1, 3, and 7. ELISA assessment was carried out according to the manufacturer's instructions and the absorbance values at 450 nm were measured with a microplate reader (Infinite F50, Tecan, Switzerland).

4.12. RNA sequencing

G@NSC, GH@NSC, and GHP@NSC ($n = 3$ in each group) were cultivated in a differentiation medium for 14 days. The total RNA of the encapsulated NSCs in 3D bio-construct was extracted using TRIzol (Invitrogen, UK) by the instructions provided by the manufacturers. Subsequently, RNA sequencing was achieved by BGI Genomics (Shenzhen, China).

4.13. Transwell experiments

Immunoregulation assessment was evaluated with indirect co-culture experiments *in vitro*. The HAPI microglia cells were cultured with Dulbecco's Modified Eagle's Medium (high glucose, DMEM, Pricella) containing 10 % FBS and 1 % PS. HAPI cells were seeded on the lower chamber of 24 well culture plates at 5×10^4 cells/well. After 12 h of adhesion, polarization medium (DMEM/F12 with 1 $\mu\text{g}/\text{mL}$ lipopolysaccharide (LPS, Invitrogen, UK) and 20 ng/mL interferon- γ (IFN- γ , Abcam, UK)) was applied to stimulate HAPI cells. Upper 0.4 μm pore insert (Labelect, China) was seeded with NSC (5×10^4 cells/well), or filled with GHP hydrogel and GHP@NSC bio-construct ($n = 3$ in each group). The blank and non-treated control group was established with and without stimulation of polarization medium, respectively. The stimulation of cells and the insert of the upper chamber were carried out spontaneously. After 24 h indirect co-culture, HAPI cells were collected and the total RNA was extracted respectively, as previously described in RT-PCR.

4.14. Animal procedures

All animal experiments in this study were carried out in strict accordance with the Guide for Care and Use of Laboratory Animals of the National Institutes of Health and were approved by the Institutional Animal Care and Use Committee of Tsinghua University (Beijing, China, approval number: 23-WXM1). Eight-week-old healthy female SD rats (200–220 g, $n = 90$) were used in this study. Rat SCI models with 4 mm-long complete transection were established as previously described [71]. Briefly, animals were anesthetized with the combination of 1 % pentobarbital sodium solution (30 mg/kg) via intraperitoneal injection. The midline dorsal skin was incised and laminectomy of T8-T10 vertebrae was performed. The dura was opened under the microscope, followed by the complete transection and removal of the 4 mm-long T9-T10 spinal cord segment. Gelfoam was applied for sufficient hemostasis, and the ventral dura matter was preserved. Afterward, animals were randomly divided into three groups for further *in vivo* study according to different treatments. Immediate implantation of GHP hydrogel construct (scaffold group, GHP group) and GHP@NSC hydrogel construct (NSC-laden construct group, GHP@NSC group) to the lesion site was carried out to fill the cavity, while the untreated control (Blank group) was established without any implant application. Finally,

muscle and skin incisions were closed with sutures in layers. After surgery, Meloxicam (4 mg/kg) and penicillin were routinely injected into the rats for three and seven days post-surgery each. All rats received abdomens massage twice daily for manual bladder extrusion until the recovery of automatic micturition. After 10 weeks post-surgery, Biotinylated dextran amines (BDA, Dextran, Alexa Fluor™ 488, 10,000 MW, D1820, Invitrogen, USA) and cholera toxin B (CTB, Alexa Fluor™ 647, C34778, Invitrogen, USA) were injected for the tract-tracing of descending propriospinal axons and ascending propriospinal axons, as demonstrated previously with slight modification [76–78]. In brief, the second laminectomy procedure was performed under anesthesia. Two segments of vertebrae rostral and caudal to the lesion site were removed. BDA anterograde (10 % w/v) was injected into the 4 sites between one and two segments rostral to the lesion site at a volume of 0.5 μL each site. CTB retrograde (1 % w/v) was injected into the 4 sites between one and two segments caudal to the lesion site at a volume of 0.5 μL each site. Injection of BDA and CTB was performed with a micropipette (Hamilton, Switzerland) at 0.15 μL per minute. Rats were sacrificed and perfused 2 weeks after the injection, spinal cord tissues were obtained for the following tract-tracing evaluation.

4.15. Motor behavior assessment

The locomotor function was assessed weekly by the movement of the hindlimb according to the Basso–Beattie–Bresnahan (BBB) rating scale by three independent scorers ($n = 6$ in each group) [79]. Twelve weeks post-surgery, the gait of the rats was recorded and evaluated with the Catwalk XT 10.6 System (Noldus, Wageningen, The Netherlands). The paw prints were labeled and analyzed further via Catwalk 10.6 software. Moreover, the rats were placed at the bottom of an inclined (45° angle from the horizontal plane) iron net to climb freely. The climbing process was recorded to assess the coordination of voluntary movement of the hindlimb.

4.16. Sensory behavior assessment

A hot/cold plate was applied for the measurement of the nociceptive threshold for the evaluation of sensory function recovery. The rats were placed on the plate heated to 55 °C, and the elapsed time that evoked nociceptive responses of the hind paw was recorded. Typical nociceptive responses are lifting or shaking the paws, jumping, and extensor spasms. Mechanical allodynia of the rats was determined with a dynamic plantar aesthesiometer (Model 37,450, Ugo Basile, and Varese, Italy). The rats ($n = 6$ in each group) were placed on the iron net, and a blunt Von-Frey-type filament with increasing force (0.2 g/s) was exerted to stimulate the hind paw. Both paws were stimulated randomly. Hind paw withdrawal or animal twitching was regarded as the threshold response. Subsequently, the exerted force was recorded and averaged per group.

4.17. Electrophysiological assessment

The motor-evoked potentials (MEPs) and somatosensory evoked potentials (SEPs) were recorded with an Electromyograph and Evoked Potential Equipment (33A07, Dantec Dynamics, Denmark). Sampling rate: 48 kHz; filter type: Bandpass; bandwidth: 0.01 Hz–13 kHz, high-pass: 0.01 Hz–3 kHz, lowpass: 20 Hz–13 kHz). Twelve-week post-surgery rats were anesthetized identically to the surgery procedure for electrophysiological assessment ($n = 3$ in each group). For MEPs, the stimulation needle electrodes were placed on the skull directly, and the recording needle electrodes were positioned in the tibialis anterior muscle of both hindlimbs. For SEPs, the stimulation electrodes were inserted into the sciatic nerve, and the recording electrodes were connected to the sensory cortex of the brain skull. For both MEPs and SEPs detection, the grounding electrode was placed into the back subcutaneously. MEPs were recorded following a single stimulation with an intensity of 45 mA and 0.1 ms pulse width. Multiple pulse stimulation

was used to produce SEPs wave with 3.5 mA intensity and 0.1 ms pulse width after averaging 200 stimulus repetitions. Further, the latency (the time interval from the end of the stimulus to the appearance of the waveform) and peak amplitude (the potential magnitude from the trough to the peak of the waveform) were analyzed and compared among groups for MEPs and SEPs.

4.18. Magnetic resonance imaging assessment

T1 and T2 weighted images (T1/2WI) and diffusion tensor images (DTI) were acquired with a 9.4 T Bruker Biospec Animal MRI System (Bruker, MA, USA). Twelve-week post-surgery rats were anesthetized identically to the surgery procedure for electrophysiological assessment. MRI data of the SCI sites were scanned and visualized to observe the recovery of the spinal cord.

4.19. Histological assessment

At 1 week, 4 weeks, and 12 weeks post-surgery, rats were sacrificed for tissue obtainment. Briefly, rats were perfused with PBS and 4 % PFA intracardially and consecutively after anesthesia, followed by the isolation and collection of spinal cord segments with the lesion epicenter. Moreover, the major organs including the heart, liver, lung, spleen, kidney, and bladder were also harvested from the rats. The collected tissue samples were fixed with 4 % PFA overnight at 4 °C and immersed in the 30 % sucrose solution for 3 days at 4 °C. Then, an optimal cutting temperature compound (OCT, Tissue-Tek OCT Compound, USA) was used to embed the tissue specimens, and a cryostat microtome (CM 1950, Leica, Germany) was utilized to cut tissue specimens into 10 μ m-thick histologic sections.

Standard hematoxylin and eosin (H&E) staining and Masson Trichrome staining were carried out with the tissue sections. Subsequently, H&E and Masson Trichrome staining images were captured with a Panoramic SCAN scanner (3DHIESTECH, Hungary). For histological immunofluorescence staining, the sections were washed with PBS, immersed in 0.3 % (w/v) Triton X-100 for 2 h and 10 % (w/v) normal goat serum for 4 h successively at room temperature. Then, the sections were bathed in primary antibodies overnight at 4 °C. After rinsing with PBS, sections were incubated with the corresponding secondary antibodies for 1 h at room temperature in the dark. DAPI mounting medium (Abcam, UK) was applied for cell nuclei staining at last. Immunofluorescence sections were observed and photographed with Zeiss Axio Scan Z1 scanner (Carl Zeiss, Germany) or scanning confocal laser microscopy (LSM980 Airyscan2, Zeiss, Germany). Images were further processed with Zen 2.6 (Blue edition) software (Carl Zeiss, Germany) under identical parameters, and quantitatively analyzed with ImageJ 1.51 k software. The representative confocal images were processed with the same illumination settings and selected from 3 rats for each group, and 3 independent areas per section as the region of interest (250 μ m × 250 μ m) including the rostral, lesion, and caudal site of the injury. The primary and secondary antibodies are presented in Table S2, Supporting Information.

Moreover, the lesion epicenters of the 12-week post-surgery rats (n = 3 in each group) were obtained for myelination evaluation. Then, the tissue segments were sliced into ultra-thin (60 nm-thick) or semi-thin (500 nm-thick) axial or transverse sections with a microtome (EM UC6, Leica, Germany). The ultra-thin sections were stained with both uranyl acetate and lead citrate and examined with a transmission electron microscope (TEM, Tecnai Spirit, FEI, Czech Republic). For semi-thin sections, toluidine blue solution was applied for staining, and a Panoramic SCAN scanner (3DHIESTECH, Hungary) was used for image acquisition. Subsequently, the representative images of TEM and toluidine blue staining were quantified and analyzed with ImageJ 1.51 k software, respectively.

At 1 week, 4 weeks, and 12 weeks post-surgery, rats (n = 3 in each group) were sacrificed and the spinal cord tissue segments were

harvested for tissue quantitative real-time PCR. Total RNA was extracted from spinal cord tissue with RNA Easy Fast Tissue/Cell Kit (Tiangen, China) and cDNA was reverse transcribed with FastKing RT kit (Tiangen, China). The qRT-PCR was performed and analyzed as above described. The primer sequences are presented in Table S1, Supporting Information.

4.20. Statistical analysis

All tests were conducted two-sided, and all data in this study is presented in the form of mean ± standard deviation. All statistical analyses were performed using the SPSS Statistics for Windows (v.23.0; IBM Corp., USA). The determination of statistical differences for multiple comparisons was evaluated by one-way factorial analysis of variance (ANOVA) followed by LSD (equal variances) or Dunnett's T3 (unequal variances) post hoc test. Repeated-measures two-way ANOVA was utilized for the comparison of significant differences among different groups and time points in the BBB experiment. Statistical significance was considered with *P < 0.05, **P < 0.01, and ***P < 0.001.

CRediT authorship contribution statement

Jia Yang: Writing – review & editing, Writing – original draft, Visualization, Project administration, Methodology, Investigation, Formal analysis, Data curation, Conceptualization. **Kunkoo Kim:** Writing – review & editing, Writing – original draft, Visualization, Software, Investigation, Data curation. **Yaosai Liu:** Writing – original draft, Validation, Methodology, Investigation. **Xiaobin Luo:** Validation, Methodology, Formal analysis, Conceptualization. **Chao Ma:** Validation, Methodology, Investigation. **Weitao Man:** Resources, Methodology, Investigation. **Yating Zhao:** Methodology, Investigation, Formal analysis. **Zheng Cao:** Project administration, Methodology, Investigation. **Peilun Hu:** Software, Formal analysis, Data curation. **Junlin Chen:** Software, Project administration, Methodology. **Yu Wang:** Resources, Project administration, Investigation. **Xiaodan Sun:** Supervision, Conceptualization. **Lingyun Zhao:** Supervision, Formal analysis. **Guihuai Wang:** Validation, Supervision, Resources, Funding acquisition, Data curation, Conceptualization. **Kaiyuan Yang:** Writing – review & editing, Writing – original draft, Supervision, Resources, Project administration, Investigation, Funding acquisition, Conceptualization. **Xiumei Wang:** Writing – review & editing, Writing – original draft, Validation, Supervision, Resources, Project administration, Methodology, Investigation, Funding acquisition, Formal analysis, Conceptualization.

Ethics approval and consent to participate

All animal experiments in this study were carried out in strict accordance with the Guide for Care and Use of Laboratory Animals of the National Institutes of Health and were approved by the Institutional Animal Care and Use Committee of Tsinghua University (Beijing, China, approval number: 23-WXM1).

Declaration of competing interest

The authors declare no competing financial interest.

Acknowledgments

The authors thank the financial support from the National Natural Science Foundation of China (Grant No. 32271414 and 82301560). The authors also thank the financial support from State Key Laboratory of New Ceramic Materials Tsinghua University (No. KF202409).

Appendix A. Supplementary data

Supplementary data to this article can be found online at <https://doi.org/10.1016/j.bioactmat.2024.12.028>.

References

- [1] M. Khorasanizadeh, M. Youseffard, M. Eskian, Y. Lu, M. Chalangari, J.S. Harrop, S. B. Jazayeri, S. Seyedpour, B. Khodaei, M. Hosseini, Neurological recovery following traumatic spinal cord injury: a systematic review and meta-analysis, *J. Neurosurg. Spine* 30 (5) (2019) 683–699.
- [2] T. Yuan, Y. Shao, X. Zhou, Q. Liu, Z. Zhu, B. Zhou, Y. Dong, N. Stephanopoulos, S. Gui, H. Yan, Highly permeable DNA supramolecular hydrogel promotes neurogenesis and functional recovery after completely transected spinal cord injury, *Adv. Mater.* 33 (35) (2021) 2102428.
- [3] I. Fischer, J.N. Dulin, M.A. Lane, Transplanting neural progenitor cells to restore connectivity after spinal cord injury, *Nat. Rev. Neurosci.* 21 (7) (2020) 366–383.
- [4] R. Matta, A.L. Gonzalez, Engineered biomimetic neural stem cell niche, *Current stem cell reports* 5 (2019) 109–114.
- [5] L. Xiao, P. Xie, J. Ma, K. Shi, Y. Dai, M. Pang, J. Luo, Z. Tan, Y. Ma, X. Wang, A bioinspired injectable, adhesive, and self-healing hydrogel with dual hybrid network for neural regeneration after spinal cord injury, *Adv. Mater.* 35 (41) (2023) 2304896.
- [6] J.G. Roth, M.S. Huang, R.S. Navarro, J.T. Akram, B.L. LeSavage, S.C. Heilshorn, Tunable hydrogel viscoelasticity modulates human neural maturation, *Sci. Adv.* 9 (42) (2023) eadh8313.
- [7] Z. Tan, L. Xiao, J. Ma, K. Shi, J. Liu, F. Feng, P. Xie, Y. Dai, Q. Yuan, W. Wu, L. Rong, L. He, Integrating hydrogels manipulate ECM deposition after spinal cord injury for specific neural reconnections via neuronal relays, *Sci. Adv.* 10(27) ead09120.
- [8] V.M. Gaspar, P. Lavrador, J. Borges, M.B. Oliveira, J.F. Mano, Advanced bottom-up engineering of living architectures, *Adv. Mater.* 32 (6) (2020) 1903975.
- [9] F. Qian, C. Zhu, J.M. Knipe, S. Ruelas, J.K. Stolaroff, J.R. DeOtte, E.B. Duoss, C. M. Spadaccini, C.A. Henard, M.T. Guarnieri, Direct writing of tunable living inks for bioprocess intensification, *Nano Lett.* 19 (9) (2019) 5829–5835.
- [10] X. Yuan, W. Zhu, Z. Yang, N. He, F. Chen, X. Han, K. Zhou, Recent advances in 3D printing of smart scaffolds for bone tissue engineering and regeneration, *Adv. Mater.* 2403641.
- [11] Y.S. Zhang, A. Dolatshahi-Pirouz, G. Orive, Regenerative cell therapy with 3D bioprinting, *Science* 385 (6709) (2024) 604–606.
- [12] X. Liu, M. Hao, Z. Chen, T. Zhang, J. Huang, J. Dai, Z. Zhang, 3D bioprinted neural tissue constructs for spinal cord injury repair, *Biomaterials* 272 (2021) 120771.
- [13] D. Joung, V. Truong, C.C. Neitzke, S.Z. Guo, P.J. Walsh, J.R. Monat, F. Meng, S. H. Park, J.R. Dutton, A.M. Parr, 3D printed stem-cell derived neural progenitors generate spinal cord scaffolds, *Adv. Funct. Mater.* 28 (39) (2018) 1801850.
- [14] J. Koffler, W. Zhu, X. Qu, O. Platoshyn, J.N. Dulin, J. Brock, L. Graham, P. Lu, J. Sakamoto, M. Marsala, Biomimetic 3D-printed scaffolds for spinal cord injury repair, *Nature medicine* 25 (2) (2019) 263–269.
- [15] J. Yang, K. Yang, W. Man, J. Zheng, Z. Cao, C.-Y. Yang, K. Kim, S. Yang, Z. Hou, G. Wang, X. Wang, 3D bio-printed living nerve-like fibers refine the ecological niche for long-distance spinal cord injury regeneration, *Bioact. Mater.* 25 (2023) 160–175.
- [16] W. Xie, X. Wei, H. Kang, H. Jiang, Z. Chu, Y. Lin, Y. Hou, Q. Wei, Static and dynamic: evolving biomaterial mechanical properties to control cellular mechanotransduction, *Adv. Sci.* 10 (9) (2023) 2204594.
- [17] C. Li, F. Meng, Z. Yang, J. Peng, Y. Guo, J. Na, Q. Shi, Y. Liu, Y. Wang, L. Zheng, Micropattern-based stem cell gym: mechanical memory enhanced stemness maintenance of human dental pulp stem cells and nerve regeneration, *Adv. Funct. Mater.* 33 (49) (2023) 2302829.
- [18] F. Urciuolo, G. Imparato, P.A. Netti, Engineering cell instructive microenvironments for in vitro replication of functional barrier organs, *Adv. Healthcare Mater.* (2024) 2400357.
- [19] K. Zhang, Q. Feng, Z. Fang, L. Gu, L. Bian, Structurally dynamic hydrogels for biomedical applications: pursuing a fine balance between macroscopic stability and microscopic dynamics, *Chem. Rev.* 121 (18) (2021) 11149–11193.
- [20] B. Yang, K. Wei, C. Loebel, K. Zhang, Q. Feng, R. Li, S.H.D. Wong, X. Xu, C. Lau, X. Chen, Enhanced mechanosensing of cells in synthetic 3D matrix with controlled biophysical dynamics, *Nat. Commun.* 12 (1) (2021) 3514.
- [21] H. De Belly, E.K. Paluch, K.J. Chalut, Interplay between mechanics and signalling in regulating cell fate, *Nat. Rev. Mol. Cell Biol.* 23 (7) (2022) 465–480.
- [22] S.M. Hull, J. Lou, C.D. Lindsay, R.S. Navarro, B. Cai, L.G. Brunel, A.D. Westerfield, Y. Xia, S.C. Heilshorn, 3D bioprinting of dynamic hydrogel bioinks enabled by small molecule modulators, *Sci. Adv.* 9 (13) (2023) eade7880.
- [23] S. Tavakoli, N. Krishnan, H. Mokhtari, O.P. Oommen, O.P. Varghese, Fine-tuning dynamic cross-linking for enhanced 3D bioprinting of hyaluronic acid hydrogels, *Adv. Funct. Mater.* 34 (4) (2024) 2307040.
- [24] K.Y. Wang, X.Y. Jin, Y.H. Ma, W.J. Cai, W.Y. Xiao, Z.W. Li, X. Qi, J. Ding, Injectable stress relaxation gelatin-based hydrogels with positive surface charge for adsorption of aggrecan and facile cartilage tissue regeneration, *J. Nanobiotechnol.* 19 (1) (2021) 214.
- [25] J. Bi, L. Zhang, P. Zhang, S. Xu, Y. Liu, X. Zhang, X. Qiu, Y. Bi, F. Yan, H. Wei, X. Cui, X. Pan, J. Huang, Y. Zhao, Nanoarchitectonics of injectable biomimetic conjugates for cartilage protection and therapy based on degenerative osteoarthritis progression, *Biomater. Res.* 28 (2024) 75.
- [26] V.D. Putra, K.A. Kilian, M.L. Knothe Tate, Biomechanical, biophysical and biochemical modulators of cytoskeletal remodelling and emergent stem cell lineage commitment, *Commun. Biol.* 6 (1) (2023) 75.
- [27] C. Ligorio, A. Mata, Synthetic extracellular matrices with function-encoding peptides, *Nature reviews bioengineering* 1 (7) (2023) 518–536.
- [28] Y. Zhang, Z. Qin, Z. Qu, M. Ge, J. Yang, Cadherin-based biomaterials: inducing stem cell fate towards tissue construction and therapeutics, *Prog. Nat. Sci.: Mater. Int.* 30 (5) (2020) 597–608.
- [29] B.N. Kharbikar, P. Mohindra, T.A. Desai, Biomaterials to enhance stem cell transplantation, *Cell Stem Cell* 29 (5) (2022) 692–721.
- [30] K. Yang, J. Yang, W. Man, Z. Meng, C.-Y. Yang, Z. Cao, J. Liu, K. Kim, Y. Liu, S. Yang, N-cadherin-functionalized nanofiber hydrogel facilitates spinal cord injury repair by building a favorable niche for neural stem cells, *Advanced Fiber Materials* 5 (4) (2023) 1349–1366.
- [31] M. Cavanaugh, R.K. Willits, Mechanotransductive N-cadherin binding induces differentiation in human neural stem cells, *Mechanobiology in Medicine* 3 (1) (2025) 100099.
- [32] Y. Li, A. Tran, L. Graham, J. Brock, M.H. Tuszynski, P. Lu, BDNF guides neural stem cell-derived axons to ventral interneurons and motor neurons after spinal cord injury, *Exp. Neurol.* 359 (2023) 114259.
- [33] Y. Li, A. Tran, L. Graham, J. Brock, M.H. Tuszynski, P. Lu, BDNF guides neural stem cell-derived axons to ventral interneurons and motor neurons after spinal cord injury, *Exp. Neurol.* 359 (2023) 114259.
- [34] R. Li, C. Zhou, J. Chen, H. Luo, R. Li, D. Chen, X. Zou, W. Wang, Synergistic osteogenic and angiogenic effects of KP and QK peptides incorporated with an injectable and self-healing hydrogel for efficient bone regeneration, *Bioact. Mater.* 18 (2022) 267–283.
- [35] W. He, Q. Wang, X. Tian, G. Pan, Recapitulating dynamic ECM ligand presentation at biomaterial interfaces: molecular strategies and biomedical prospects. *Exploration*, Wiley Online Library, 2022 20210093.
- [36] F. Feng, X. Song, Z. Tan, Y. Tu, L. Xiao, P. Xie, Y. Ma, X. Sun, J. Ma, L. Rong, Cooperative assembly of a designer peptide and silk fibroin into hybrid nanofiber gels for neural regeneration after spinal cord injury, *Sci. Adv.* 9 (25) (2023) eadg0234.
- [37] F. Zhu, N. Yan, X. Lu, J. Xu, H. Gu, J. Liang, K. Cheng, X. Wang, X. Ma, N. Ma, Cell-reprogramming-inspired dynamically responsive hydrogel boosts the induction of pluripotency via phase-separated biomolecular condensates, *Adv. Mater.* 36 (22) (2024) 2211609.
- [38] W. Xie, X. Wei, H. Kang, H. Jiang, Z. Chu, Y. Lin, Y. Hou, Q. Wei, Static and dynamic: evolving biomaterial mechanical properties to control cellular mechanotransduction, *Adv. Sci.* 10 (9) (2023) e2204594.
- [39] C. Ligorio, A. Mata, Synthetic extracellular matrices with function-encoding peptides, *Nat Rev Bioeng* (2023) 1–19.
- [40] W. He, Q. Wang, X. Tian, G. Pan, Recapitulating dynamic ECM ligand presentation at biomaterial interfaces: molecular strategies and biomedical prospects, *Explorations* 2 (1) (2022) 20210093.
- [41] O. Chaudhuri, J. Cooper-White, P.A. Janmey, D.J. Mooney, V.B. Shenoy, Effects of extracellular matrix viscoelasticity on cellular behaviour, *Nature* 584 (7822) (2020) 535–546.
- [42] J. Baek, P.A. Lopez, S. Lee, T.-S. Kim, S. Kumar, D.V. Schaffer, Egr 1 is a 3D matrix-specific mediator of mechanosensitive stem cell lineage commitment, *Sci. Adv.* 8 (15) (2022) eabm4646.
- [43] O. Chaudhuri, L. Gu, D. Klumpers, M. Darnell, S.A. Bencherif, J.C. Weaver, N. Huebsch, H.-p. Lee, E. Lippens, G.N. Duda, Hydrogels with tunable stress relaxation regulate stem cell fate and activity, *Nat. Mater.* 15 (3) (2016) 326–334.
- [44] S. Taheri, G. Bao, Z. He, S. Mohammadi, H. Ravanbakhsh, L. Lessard, J. Li, L. Mongeau, Injectable, pore-forming, perfusable double-network hydrogels resilient to extreme biomechanical stimulations, *Adv. Sci.* 9 (2) (2022) 2102627.
- [45] Y. Ren, X. Yang, Z. Ma, X. Sun, Y. Zhang, W. Li, H. Yang, L. Qiang, Z. Yang, Y. Liu, Developments and opportunities for 3D bioprinted organoids, *International Journal of Bioprinting* 7 (3) (2021).
- [46] J.M. Taylor, S. Cohen, W.M. Mitchell, Epidermal growth factor: high and low molecular weight forms, *Proc. Natl. Acad. Sci. USA* 67 (1) (1970) 164–171.
- [47] J. Baek, S. Kumar, D.V. Schaffer, S.G. Im, N-Cadherin adhesive ligation regulates mechanosensitive neural stem cell lineage commitment in 3D matrices, *Biomater. Sci.* 10 (23) (2022) 6768–6777.
- [48] A. Rodrigo-Navarro, S. Sankaran, M.J. Dalby, A. del Campo, M. Salmeron-Sanchez, Engineered living biomaterials, *Nat. Rev. Mater.* 6 (12) (2021) 1175–1190.
- [49] B.D. Cosgrove, K.L. Mui, T.P. Driscoll, S.R. Caliar, K.D. Mehta, R.K. Assoian, J. A. Burdick, R.L. Mauck, N-cadherin adhesive interactions modulate matrix mechanosensing and fate commitment of mesenchymal stem cells, *Nat. Mater.* 15 (12) (2016) 1297–1306.
- [50] W. Man, S. Yang, Z. Cao, J. Lu, X. Kong, X. Sun, L. Zhao, Y. Guo, S. Yao, G. Wang, A multi-modal delivery strategy for spinal cord regeneration using a composite hydrogel presenting biophysical and biochemical cues synergistically, *Biomaterials* 276 (2021) 120971.
- [51] B.Y. Chen, X. Wang, Z.Y. Wang, Y.Z. Wang, L.W. Chen, Z.J. Luo, Brain-derived neurotrophic factor stimulates proliferation and differentiation of neural stem cells, possibly by triggering the Wnt/ β -catenin signaling pathway, *J. Neurosci. Res.* 91 (1) (2013) 30–41.
- [52] B. Chen, Z. Xiao, Y. Zhao, J. Dai, Functional biomaterial-based regenerative microenvironment for spinal cord injury repair, *Natl. Sci. Rev.* 4 (4) (2017) 530–532.
- [53] P. Popovich, D. McTigue, Damage control in the nervous system: beware the immune system in spinal cord injury, *Nature medicine* 15 (7) (2009) 736–737.

- [54] C.S. Ahuja, J.R. Wilson, S. Nori, M. Kotter, C. Druschel, A. Curt, M.G. Fehlings, Traumatic spinal cord injury, *Nat. Rev. Dis. Prim.* 3 (1) (2017) 1–21.
- [55] S. Yao, Y. Yang, C. Li, K. Yang, X. Song, C. Li, Z. Cao, H. Zhao, X. Yu, X. Wang, Axon-like aligned conductive CNT/GelMA hydrogel fibers combined with electrical stimulation for spinal cord injury recovery, *Bioact. Mater.* 35 (2024) 534–548.
- [56] T.J. Dause, J.K. Denninger, B.M. Smith, E.D. Kirby, The neural stem cell secretome across neurodevelopment, *Exp. Neurol.* 355 (2022) 114142.
- [57] L. Peruzzotti-Jametti, J.D. Bernstock, N. Vicario, A.S. Costa, C.K. Kwok, T. Leonardi, L.M. Booty, I. Bicci, B. Balzarotti, G. Volpe, Macrophage-derived extracellular succinate licenses neural stem cells to suppress chronic neuroinflammation, *Cell Stem Cell* 22 (3) (2018) 355–368, e13.
- [58] M. Liu, W. Zhang, S. Han, D. Zhang, X. Zhou, X. Guo, H. Chen, H. Wang, L. Jin, S. Feng, Multifunctional conductive and electrogenic hydrogel repaired spinal cord injury via immunoregulation and enhancement of neuronal differentiation, *Adv. Mater.* (2024) 2313672.
- [59] A.P. Tran, P.M. Warren, J. Silver, The biology of regeneration failure and success after spinal cord injury, *Physiol. Rev.* 98 (2) (2018) 881–917.
- [60] B.T. Lang, J.M. Cregg, M.A. DePaul, A.P. Tran, K. Xu, S.M. Dyck, K.M. Madalena, B. P. Brown, Y.-L. Weng, S. Li, Modulation of the proteoglycan receptor PTP α promotes recovery after spinal cord injury, *Nature* 518 (7539) (2015) 404–408.
- [61] M.L. Kutys, C.S. Chen, Forces and mechanotransduction in 3D vascular biology, *Curr. Opin. Cell Biol.* 42 (2016) 73–79.
- [62] J. Whisler, S. Shahreza, K. Schlegelmilch, N. Ege, Y. Javanmardi, A. Malandrino, A. Agrawal, A. Fantin, B. Serwinski, H. Azizgolshani, C. Park, V. Shone, O.O. Demuren, A. Del Rosario, V.L. Butty, N. Holroyd, M.-C. Domart, S. Hooper, N. Szita, L.A. Boyer, S. Walker-Samuel, B. Djordjevic, G.K. Sheridan, L. Collinson, F. Calvo, C. Ruhrberg, E. Sahai, R. Kamm, E. Moendarbary, Emergent mechanical control of vascular morphogenesis, *Sci. Adv.* 9(32) eadg9781.
- [63] G.L. Barrett, P.F. Bartlett, The p75 nerve growth factor receptor mediates survival or death depending on the stage of sensory neuron development, *Proc. Natl. Acad. Sci. USA* 91 (14) (1994) 6501–6505.
- [64] M. Canossa, J.L. Twiss, A.N. Verity, E.M. Shooter, p75 (NGFR) and TrkA receptors collaborate to rapidly activate a p75 (NGFR)-associated protein kinase, *EMBO J.* 15 (13) (1996) 3369–3376.
- [65] E.J. Huang, L.F. Reichardt, Trk receptors: roles in neuronal signal transduction, *Annu. Rev. Biochem.* 72 (1) (2003) 609–642.
- [66] H.S. Gilmer-Hill, R. Beuerman, Q. Ma, J. Jiang, R.L. Tiel, D.G. Kline, Response of GAP-43 and p75 in human neuromas over time after traumatic injury, *Neurosurgery* 51 (5) (2002) 1229–1238.
- [67] S.-K. Lee, S.L. Pfaff, Transcriptional networks regulating neuronal identity in the developing spinal cord, *Nat. Neurosci.* 4 (Suppl 11) (2001) 1183–1191.
- [68] X. Hu, W. Xu, Y. Ren, Z. Wang, X. He, R. Huang, B. Ma, J. Zhao, R. Zhu, L. Cheng, Spinal cord injury: molecular mechanisms and therapeutic interventions, *Signal Transduct. Targeted Ther.* 8 (1) (2023) 245.
- [69] C. Stadelmann, S. Timmler, A. Barrantes-Freer, M. Simons, Myelin in the central nervous system: structure, function, and pathology, *Physiol. Rev.* 99 (3) (2019) 1381–1431.
- [70] B.-Q. Lai, X. Zeng, W.-T. Han, M.-T. Che, Y. Ding, G. Li, Y.-S. Zeng, Stem cell-derived neuronal relay strategies and functional electrical stimulation for treatment of spinal cord injury, *Biomaterials* 279 (2021) 121211.
- [71] J. Yang, K. Yang, W. Man, J. Zheng, Z. Cao, C.-Y. Yang, K. Kim, S. Yang, Z. Hou, G. Wang, 3D bio-printed living nerve-like fibers refine the ecological niche for long-distance spinal cord injury regeneration, *Bioact. Mater.* 25 (2023) 160–175.
- [72] C. Cai, X. Zhang, Y. Li, X. Liu, S. Wang, M. Lu, X. Yan, L. Deng, S. Liu, F. Wang, Self-healing hydrogel embodied with macrophage-regulation and responsive-gene-silencing properties for synergistic prevention of peritendinous adhesion, *Adv. Mater.* 34 (5) (2022) 2106564.
- [73] X. Wang, X.H. Qin, C. Hu, A. Terzopoulou, X.Z. Chen, T.Y. Huang, K. Maniura-Weber, S. Pané, B.J. Nelson, 3D printed enzymatically biodegradable soft helical microswimmers, *Adv. Funct. Mater.* 28 (45) (2018) 1804107.
- [74] M. Liu, R. Ding, Z. Li, N. Xu, Y. Gong, Y. Huang, J. Jia, H. Du, Y. Yu, G. Luo, Hyaluronidase-responsive bactericidal cryogel for promoting healing of infected wounds: inflammatory attenuation, ROS scavenging, and immune regulation, *Adv. Sci.* 11 (17) (2024) 2306602.
- [75] R. Tao, T.-J. Sun, Y.-Q. Han, G. Xu, J. Liu, Y.-F. Han, Optimization of in vitro cell labeling methods for human umbilical cord-derived mesenchymal stem cells, *Eur. Rev. Med. Pharmacol. Sci.* 18 (8) (2014).
- [76] R. Muramatsu, C. Takahashi, S. Miyake, H. Fujimura, H. Mochizuki, T. Yamashita, Angiogenesis induced by CNS inflammation promotes neuronal remodeling through vessel-derived prostacyclin, *Nat Med* 18 (11) (2012) 1658–1664.
- [77] Y. Yang, Y. Fan, H. Zhang, Q. Zhang, Y. Zhao, Z. Xiao, W. Liu, B. Chen, L. Gao, Z. Sun, X. Xue, M. Shu, J. Dai, Small molecules combined with collagen hydrogel direct neurogenesis and migration of neural stem cells after spinal cord injury, *Biomaterials* 269 (2021) 120479.
- [78] S. Liu, B. Sandner, T. Schackel, L. Nicholson, A. Chtarto, L. Tenenbaum, R. Puttagunta, R. Müller, N. Weidner, A. Blesch, Regulated viral BDNF delivery in combination with Schwann cells promotes axonal regeneration through capillary alginate hydrogels after spinal cord injury, *Acta Biomater.* 60 (2017) 167–180.
- [79] D.M. Basso, M.S. Beattie, J.C. Bresnahan, A sensitive and reliable locomotor rating scale for open field testing in rats, *J. Neurotrauma* 12 (1) (1995) 1–21.